DISCLAIMER

LASER-ULTRASOUND CHARACTERIZATION OF SPHERICAL OBJECTS

by

Chung-kao Peter Hsieh

G. L. Report No. 5097

A DISSERTATION
SUBMITTED TO THE DEPARTMENT OF AERONAUTICS AND ASTRONAUTICS
AND THE COMMITTEE ON GRADUATE STUDIES
OF STANFORD UNIVERSITY
IN PARTIAL FULFILLMENT OF THE REQUIRMENTS
FOR THE DEGREE OF
DOCTOR OF PHILOSOPHY

June 1993

Edward L. Ginzton Laboratory
Stanford University
Stanford, CA 94305-4085

FG03-84ER45157

I certify that I have read this dissertation and that in my opinion it is fully adquate, in scope and quality, as a dissertation for the degree of Doctor of Philosophy.

Butrus T. Khuri-Yakub (Principal Advisor)

I certify that I have read this dissertation and that in my opinion it is fully adquate, in scope and quality, as a dissertation for the degree of Doctor of Philosophy.

Gordon S. Kino

I certify that I have read this dissertation and that in my opinion it is fully adquate, in scope and quality, as a dissertation for the degree of Doctor of Philosophy.

Fu-Kuo Chang

Approved for the University Committee on Graduate Studies:

LASER-ULTRASOUND CHARACTERIZATION OF SPHERICAL OBJECTS

Chung-kao Peter Hsieh, Ph. D.

Stanford University, 1993

Ceramic bearing balls are desirable for use in high temperature and nonlubricative environments because of their ability to retain high mechanical strength and reduced wear. However, because ceramics are brittle, it is very important to inspect ceramic parts for the existence of small (1-10 μm) surface defects. The resonance spectrum of a spherical object can provide information about its material properties such as shear and longitudinal wave velocities to a high degree of accuracy. Also, surface wave resonant modes that are observed at high frequencies (the half circumference of the sphere is a multiple of at least 100 times the half surface wavelength) provide information about the surface cracks density. As surface waves encounter a defect, the resonant energy will be attenuated. By comparing the surface wave mode Quality factors (Q) between a perfect and an imperfect sphere, we are able to quickly detect the existence of surface imperfection. We find that a single defect will reduce the surface wave resonant Q by about 30%.

A non-contacting detection scheme is desired because contacting points will also attenuate surface wave energy and make the detection of surface cracks less sensitive. We present here a non-contacting detection method to measure resonances of a sphere. In this case, we constructed a computer controlled system to excite resonances on a

sphere with a transducer by a single Hertzian contact, and we use an optical Heterodyne interferometer to detect both amplitude and phase of the surface variations on the opposite pole of the sphere. This system is capable of inspecting bearing balls with diameters ranging from 12 mm to 1 mm.

Acknowledgments

Many people contributed to the realization of the thesis. I would like to first thank my advisor, Professor B. T. Khuri-Yakub, for giving me the opportunity to learn from and to work with him. During my career at Stanford, I learned not only about science but also about life from him. His great physical insight and constant encouragement have guided me throughout this research. I would also like to thank to Professor G. S. Kino for exciting discussions about physics and theories of wave propagation and for being a reader of this thesis.

I would next like to express my gratitude to Professor F. K. Chang for agreeing to be a reader of this thesis. I thank Professor D. Bershader, and Professor D. Beach for agreeing to be members of my committee.

I would like to thank Dr. C-H Chou for helping me during my beginning years in Ginzton laboratory. I would especially like to thank Dr. Fred Stanke and Dr. Kenneth Liang at Schlumberger Dolls Research for giving me two fruitful summer job experiences.

The K/KY group has made my stay at Ginzton a good time. Time shared together was not only about science but about life and philosophy. I am sure this will build up a long lasting friendship. They are Sanjay Bahardwaj, Fang-Cheng Chang, Can Cinbis, Stanley Chim, Levent Degertekin, Dave Dickensheets, Evan Green, Matt Haller, Duff Howell, Yongjin Lee, Alice Liu, Jun Pei, Bill Studenmund, and Xiao-Dong Wu. Especially Sanjay who helped me setting up the interferometer system and Matt who helped me a lot on the electronics and kindly used his Matlab transducer modelling program to calculate transducer surface displacement for me in Chapter 4.

I want to acknowledge the help I got from Ginzton members, especially Ingrid Tarien for a lot of paper work, Ted Bradshaw for teaching me machining skills, Tom Carver, Joe Vrhel, and Chris Ramen for a lot of technical assistance.

Finally, I wish to thank my family for their love and support throughout the years. I deeply thank my parents for weekly international phone call support. I would deeply express my gratitude and love to my wife Ting-Yi, her support, encouragement and love always make life so much more enjoyable.

Table of Contents

List of Tables

Table **Page**

List of Illustrations

Figure **Page**

Chapter 1

Introduction

1.1 Introduction

1.1.1 Importance of Ceramic Materials

Among the new discoveries and developments of science and technology in the last few decades, which include an unprecedented number of new materials and applications, are ceramics materials. Because of their unique performance and cost competitiveness, ceramics have an important role as the most suitable substitutes in traditional applications and as new functional materials for innovative technology systems. Research tools and knowledge from powder metallurgy have been appraised and adapted to the field, as has experience gained from the classical ceramics industry; and novel sophisticated physical and chemical routes to ceramics processing and characterization have been introduced. This has resulted in improved processing techniques, novel materials, and the opening of new frontiers to research and applications.[1]

Ceramic products touch our lives in many ways. Pottery and porcelain vessels, glass and cement are only among the more familiar. Their applications include the magnets in television sets, optical fibers for telecommunications, automobile spark plugs, and the insulators for power transmission lines and Japan's high-speed trains. They are widely used in electronics, not only as magnets and as insulators, but also as heating elements and substrates for integrated circuits. In bioceramics, they are used for artificial teeth and bones. As engineering ceramics, they appear in ceramic engines and cutting tools.[2]

1.1.2 Definitions of Ceramics

As a result of the high rate of technology development, there arises a need to formulate a definition of the term 'ceramics'. According to D. E. Dodd's *Dictionary of Ceramics*, the following definition applies:[3]

> Ceramic. The usual derivation is from *Keramos*, the Greek work for potters' clay or ware made from clay and fired; by a natural extension of meaning, the term has for long embraced all products made from fired clay, i.e., bricks and tiles, pipes and fireclay refractories, sanitary-ware and electrical porcelain, as well as pottery tableware. In 1822 silica refractories were first made; they contained no clay, but were made by the normal ceramic process of shaping a moist batch, drying the shaped ware and firing it. The word 'ceramic', while retaining its original sense of a product made from clay, thus tacitly began to include other products made by the same general process of manufacture. There has in consequence been no difficulty in permitting the term to embrace the many new non-clay materials now being used in electrical, nuclear and high-temperature engineering.

In the USA a radical extension of meaning was authorized by the American Ceramic Society in 1920; chemically, clay is a silicate and it was proposed that the term 'ceramic' should be applied to all the silicate industries; this brought in glass, vitreous enamel, and hydraulic cement. In Europe, this wider meaning of the word has not yet been fully accepted.

Technological change is also forcing changes in the limits placed on the term 'ceramics'. Generally speaking, ceramics are a class of inorganic, refractory materials with extremely useful structural and electrical properties as well as being applicable in familiar applications such as eating utensils.

Structural ceramics, such as silicon nitride (Si_3N_4) and silicon carbide (SiC), are desirable for use because of their high mechanical strength at high temperature and in nonlubricative environments. These materials also exhibit good corrosion resistance and are light in weight relative to most metals used in structural applications. These are the properties that make ceramics attractive for use in high temperature applications, as in components for internal combustion engines, bearings, gas turbines, cutting tools and other devices. This category of ceramic materials is the one of interest in this work. This thesis deals with the non-destructive inspection for surface defects on ceramic bearing balls.

1.2 Inspection of Ceramic Materials

1.2.1 The Importance of the Inspection of Ceramic Materials

The brittle nature of ceramics and consequent susceptibility to fracture initiated from stress concentrating flaws, either internal or external, can offset many of the more attractive properties of these materials Under load or wear conditions, a defect can cause total mechanical failure of the entire structure. Although improvements in processing technologies have greatly reduced the occurrence and severity of internal defects, it is very important to inspect ceramic parts for the existence of small (1-10 μm) defects on the surface. The evolution of techniques for detecting and characterizing cracks is thus necessary for reliable failure prediction.

The use of ultrasonic waves as a quantitative tool in nondestructive testing of materials for defects has received considerable attention in recent years. There has been significant development in experimental techniques as well as advances in theories describing the interaction between acoustic waves with various types of flaws. Among these advances is the use of surface acoustic waves (SAW or Rayleigh waves)[4,5,6] in the inspection of surface defects.

In this thesis, we discuss issues of the characterization of ceramic bearing balls. The problem of inspecting surface defects of ceramic bearing balls remains a difficult one. Little research has been done on the subject of surface waves propagating on spheres, or other objects of odd geometries. The theoretical difficulty lies in the mathematical treatment of surface acoustic waves propagating around a sphere, a resonant case. On the experimental side, the difficulties lie in the excitation and detection of surface waves on a sphere, especially on small spheres, for which the handling and change of orientation are very difficult to control.

1.2.2 Current Inspection Techniques

Current inspection of ceramic bearing balls involve visual inspection, resonant ultrasound spectroscopy, and acoustic microscopy. In the case of visual of inspection, a human operator manually rotates the sphere and inspects it under an ordinary optical microscope. The process of completing the inspection of one ball typically takes up to 30 minutes. Consequently, human factors such as fatigue make this inspection technique unreliable.

A group in Los Alamos National Laboratory has also developed a resonant ultrasound spectroscopic technique to perform non-destructive inspection on spherical objects[7]. By observing the resonance spectrum of the lowest resonant mode, they claimed to be able to observe the existence of defects. However, low frequency measurement results are not reliable for detecting the existence of defects, as will be discussed later with our experimental results in chapter 3.

In the Ginzton Laboratory, we have developed and used an acoustic microscope that operates in the frequency range of 1-200MHz. This microscope is capable of measuring amplitude and phase associated with defects on ceramic bearing balls[8,9]. This microscope provides clear images of surface damage with lateral sizes smaller than the wavelength. Figure 1.1 shows three images taken by the microscope. The field of view is 1mm x 1mm. The operating frequency is 112MHz, the lens aperture 1mm, and the focal length is 1mm (F# =1). Fringes are due to the spherical shape of the sample being observed.

The three pictures are images of the same bearing ball, the first is taken with the lens focused on the top of the surface, the second is taken at a defocused distance of 10μm by bringing the lens closer to the sample, and the third is defocused by 100μm. It is observed that the defect becomes more apparent when defocused, while the image of the dust (the round shadow) is sharpest when the microscope is focused on the top.

The acoustic microscope, though provides accurate images of the surface of the sphere, cannot cover the entire surface without several rotations of the sphere. This procedure not only is time consuming but also becomes especially cumbersome for small spheres.

The three current inspection techniques are either unreliable or time consuming or both. Therefore, it is important to develop a technique to be able to perform quality control of ceramic bearing balls more efficiently and reliably.

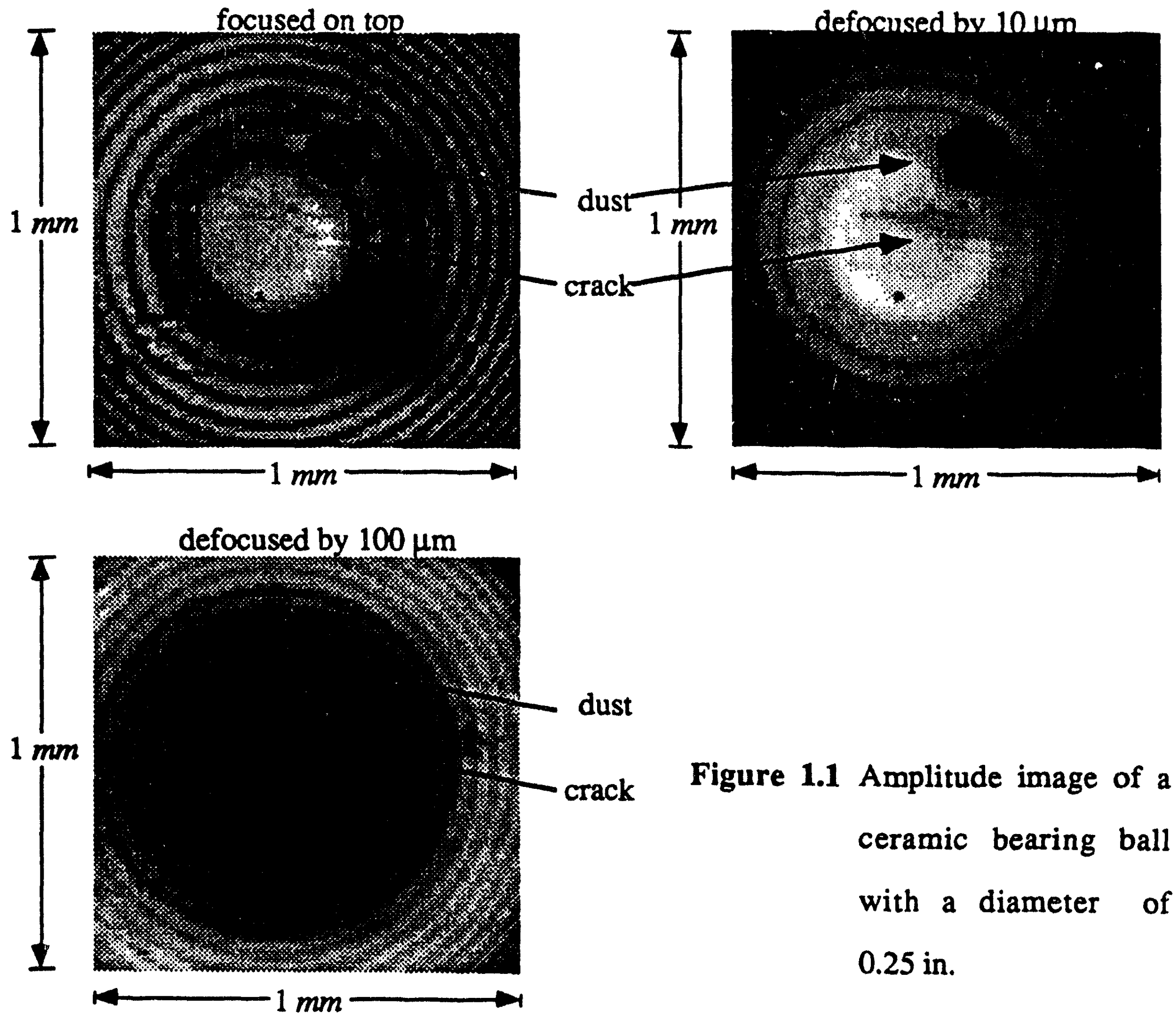

Figure 1.1 Amplitude image of a ceramic bearing ball with a diameter of 0.25 in.

1.3 Summary of Theory and Experiment

Continuous waves on a finite structure such as spheres form standing waves. At certain frequencies, these standing waves will form resonances on the objects. Resonance contains information of the whole mechanical system which in our case, is the ceramic bearing ball. Therefore, by exciting resonances on the ball, we should be able to get information about its entire structure. Generally speaking, there are two types of waves propagating on a ceramic bearing ball, longitudinal waves and shear waves. We shall show later in Chapter 2 that it is possible to excite two types of resonances on a sphere, the spheroidal resonances and the torsional resonances. The former is generated by a combination of a longitudinal waves and a shear waves, the latter is formed by a pure shear waves. We shall also show that in the high frequency region, surface wave resonances (a special case of the spheroidal resonance) can be generated and used for surface defect inspection.

The resonant sphere technique was developed in 1964 by D. B. Fraser.[10] to characterize material acoustic properties such as longitudinal wave velocity, shear wave velocity, and Poisson's ratio. As we will show in Chapter 2, the resonance frequencies of a sphere can be theoretically calculated given its radius and the longitudinal wave velocity, and shear wave velocity, or Poisson's ratio. Therefore, the inverse problem of calculating the acoustic properties of a sphere given experimentally measured resonance frequency data and the sphere's radius becomes trivial. The technique developed by Fraser was operated in the low frequency region where the resonance modes are more easily identified (theoretically the higher frequency spectrum is very complicated because of higher order harmonics). This technique was adopted by several other research groups[11,12], but all limited its use in the low frequency region to material property measurement.

This thesis describes broader applications and improvements over the original resonant sphere technique. We will show its application in both low and high frequency regions. In the low frequency region, we are able to characterize material properties to a high degree of accuracy. In the high frequency region, we show experimentally, for the first time, the existence of surface wave resonances on a sphere. We then use the surface waves to characterize the existence of surface flaws on spheres.

In Chapter 2, we discuss and summarize the theory of Rayleigh wave propagation. We then show that there are two different types of resonance modes on a sphere, the spheroidal resonances and the torsional resonances. The spheroidal resonances are caused by a combination of longitudinal and shear waves, while the torsional resonances are caused by shear waves only. We will also consider one of the special cases of the spheroidal resonances — surface acoustic wave resonance on spheres. We then use Green's function theory[13] to discuss an important phenomenon of surface wave propagation on spheres — focusing. The understanding of this phenomenon helps us establish the criteria for the excitation and detection of surface waves on spheres later in chapters 3 and 4.

In chapter 3 we discuss a variation and improvement of the resonant sphere technique — the contact-contact resonant sphere technique. Two transducers in light contact with the ball at the opposite poles act as a transmitter-receiver pair. Because of the focusing effect of surface waves on a sphere, we choose the focal points (two opposite poles) of the surface waves to be our contacting points. We show the application of this technique in the low frequency region — measurement of material properties. We then discuss the experimental observation of surface wave resonances at high frequencies and how surface waves on a sphere can be used to detect surface defects.

In chapter 4 we will describe a laser-ultrasound measurement system. We developed a laser-ultrasound system that can measure the resonance spectrum of spheres from 10 KHz to 70 MHz. We manufactured a special type of transducer that supports the sphere and excites resonances on the sphere through only one contacting point. The resonance spectrum of the sphere is detected by a non-contacting broadband optical detection scheme on the opposite pole of the sphere. We demonstrated high accuracy in the measurement of acoustic properties using this system. We demonstrated also the use of surface waves to perform non-destructive evaluation of spheres.

In chapter 5 we will give a brief summary of the experimental results and discuss future applications and possible improvements to the current technique.

References

[1] P. Vincenaini, *Fundamentals of Ceramic Engineering*, Elsevier Applied Science, London (1991)

[2] Shigeyuki Somiya, *Advanced Technical Ceramics*, Academic Press, Inc., Tokyo (1984)

[3] D. E. Dodd, *Dictionary of Ceramics*, Elsevier, Amsterdam (1964).

[4] Lord Rayleigh, *On Waves Propagated Along the Plane Surfaces of an Elastic Solid*, Proc. London Math. Soc., **17**, 4-11 (1885).

[5] J. J. Tien, *Surface Acoustic Wave Probing of Ceramics*, Ph.D. dissertation, Stanford University, 1983.

[6] M. T. Resch, *Non-Destructive Evaluation of Small Surface Cracks Using Surface Acoustic Waves*, Ph. D. dissertation, Stanford University, 1982.

[7] A. Migliori, T. M. Bell, R. D. Dixon, and R. Strong, *Resonant Ultrasound Non-Destructive Inspection*, Los Alamos National Laboratory Technical Report LA-UR-95-225.

[8] P. Parent, C-H. Chou, and B. T. Khuri-Yakub, *Ball Bearing Inspection with an Acoustic Microscope*, Proc. IEEE Ultrasonics Symposium (1988).

[9] C-H. Chou, C. P. Hsieh, and B. T. Khuri-Yakub, *Amplitude and Phase Acoustic Microscopy for Ceramic Bearing Ball Inspections*, Proc. IEEE Ultrasonics Symposium (1990).

[10] D. B. Fraser and R. C. LeCraw, *Novel Method of Measuring Elastic and Anelastic Properties of Solids*, Rev. Sci. Inst. **35**, 1113-1115 (1964).

[11] Naohiro Soga and Orson L. Anderson, *Elastic Properties of Tektites Measured by Resonant Sphere Technique*, J. Geoph. Res. **72**, 1733-1739 (1967)

[12] M. R. Notis, R. M. Spriggs, and W. C. Hahn, Jr., *Elastic Moduli of Pressure-Sintered Nickel Oxide*, J. Geoph. Res. **76**, 7052-7061 (1971).

[13] G. S. Kino, *Acoustic Waves: Devices, Imaging, and Analog Signal Processing* Prentice-Hall, New Jersey, (1987).

Chapter 2

Theories of Rayleigh Waves and Spherical Resonances

2.1 Introduction

In this chapter, we will discuss theories of Rayleigh waves[1] and spherical resonances. Rayleigh waves have been shown to be capable of the detection of surface defects on planar surfaces.[2,3] and have attracted applications in the field of non-destructive testing (NDT) during the past decade. For the case of a sphere, Rayleigh waves exist only at high frequencies where the radius of curvature of the sphere is relatively large compared to the wavelength.

Resonances on a sphere can be categorized into two types: the spheroidal resonances and the torsional resonances. A spheroidal resonance is generated by a combination of shear waves and longitudinal waves, while a torsional resonance is generated by shear waves only. Since resonances are formed by standing waves, there is a relationship between Rayleigh waves on a sphere and spherical resonances. As will be shown later in this chapter, Rayleigh wave resonances on a sphere are just a special case of the spheroidal resonance, and only exist at high frequencies.

The theory of Rayleigh wave propagation on a planar surface is familiar in the field of non-destructive evaluation because of its wide usage. We will only try to summarize this theory briefly in this chapter. Interested readers are referred to a famous book by I. A. Viktorov called *Rayleigh and Lamb Waves*.[4] This book discusses in great detail the theory of Rayleigh wave propagation. Spherical resonances, on the other hand, are unfamiliar to the NDT community, and will be discussed in greater detail in this chapter. The relationship between spherical resonances and Rayleigh waves will also be discussed.

2.2 Rayleigh Wave Theory

The propagation of acoustic waves on the surface of a semi-infinite medium with stress-free boundary condition was first described by Lord Rayleigh in 1885[5]. These waves are called Rayleigh waves or Surface Acoustic Waves (SAW). Rayleigh wave propagation is confined to vicinity of the free boundary with wave amplitudes decaying rapidly with increasing depth below the solid surface. The theory of Rayleigh wave propagation on planar surfaces has been studied in great detail. We will only summarize this theory briefly in this section[6].

Consider a linear elastic half space which occupies the region $y > 0$, with a free surface at $y = 0$ as shown in Figure 2.1. The surface of the half space lies in the x - z

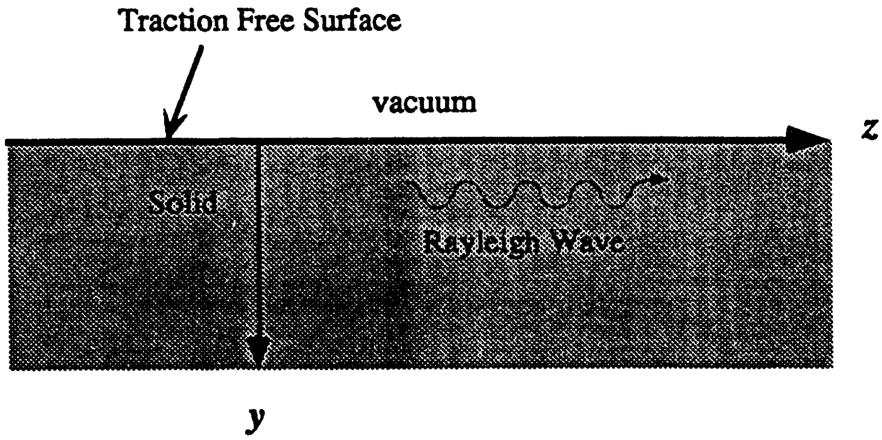

Figure 2.1 Configuration for Rayleigh wave analysis

plane. For isotropic materials, the mechanical displacement $\boldsymbol{u}$ can be expressed in terms of a scalar potential Φ and a vector potential $\boldsymbol{\Psi}$.

$$\boldsymbol{u} = \nabla\Phi + \nabla \times \boldsymbol{\Psi} \tag{2.1}$$

We associate the potential Φ with the longitudinal component of motion, and the vector potential $\boldsymbol{\Psi}$ with the shear component of motion. For motions that are independent of the coordinate x, the $\nabla \times \boldsymbol{\Psi}$ term in equation (2.1) tells us that only the x coordinate of $\boldsymbol{\Psi}$ can be finite, and we write:

$$\boldsymbol{\Psi} = \psi\hat{\boldsymbol{x}}. \tag{2.2}$$

The two potentials Φ and Ψ satisfy Helmholtz's equations[7], separately:

$$\left(\nabla^2 + k_l^2\right)\Phi = 0 \tag{2.3}$$

$$\left(\nabla^2 + k_s^2\right)\Psi = 0 \tag{2.4}$$

where

$$k_l = \omega\sqrt{\rho/(\lambda + 2\mu)} = \omega / V_l \tag{2.5}$$

$$k_s = \omega\sqrt{\rho/\mu} = \omega / V_s \tag{2.6}$$

where ω is the angular frequency, ρ is the mass density, λ and μ are the Lamé constants of the material, V_l and V_s are the acoustic velocities of the longitudinal and shear waves.

Again, for propagation that is independent of the coordinate x, equations (2.3) and (2.4) can be written as

$$\frac{\partial^2\Phi}{\partial z^2} + \frac{\partial^2\Phi}{\partial y^2} + k_l^2\Phi = 0 \tag{2.7}$$

$$\frac{\partial^2\Psi}{\partial z^2} + \frac{\partial^2\Psi}{\partial y^2} + k_s^2\Psi = 0 \tag{2.8}$$

Solutions to equations (2.7) and (2.8) have the general form:

$$\Phi = Ae^{-j(k_R - \omega t) - qy} \tag{2.9}$$

and

$$\Psi = Be^{-j(k_R - \omega t) - sy} \tag{2.10}$$

where k_R is the wave number of the Rayleigh wave, A and B are constants, and the quantities q and s are given by

$$q^2 = k_R^2 - k_l^2 \tag{2.11}$$

and

$$s^2 = k_R^2 - k_s^2 \tag{2.12}$$

If we look for solutions that fall off exponentially to as $y \to \infty$, q and s must be the positive roots of the above two equations.

The boundary condition of Rayleigh waves requires traction free on the free surface $y = 0$. The expression for stress is obtained by first finding the displacement expression and then utilizing the stress-strain relationship. From equation (2.1), we get expressions for displacement as follows:

$$u_z = \frac{\partial \Phi}{\partial z} - \frac{\partial \psi}{\partial y} \tag{2.13}$$

and

$$u_y = \frac{\partial \Phi}{\partial y} + \frac{\partial \psi}{\partial z} \tag{2.14}$$

Equations (2.13) and (2.14) can be used to determine the stress components in the medium given by the stress-strain relationship for isotropic materials[8]:

$$\begin{bmatrix} \sigma_{xx} \\ \sigma_{yy} \\ \sigma_{zz} \\ \sigma_{yz} \\ \sigma_{xz} \\ \sigma_{xy} \end{bmatrix} = \begin{bmatrix} \lambda+2\mu & \lambda & \lambda & 0 & 0 & 0 \\ \lambda & \lambda+2\mu & \lambda & 0 & 0 & 0 \\ \lambda & \lambda & \lambda+2\mu & 0 & 0 & 0 \\ 0 & 0 & 0 & \mu & 0 & 0 \\ 0 & 0 & 0 & 0 & \mu & 0 \\ 0 & 0 & 0 & 0 & 0 & \mu \end{bmatrix} \begin{bmatrix} \partial u_x / \partial x \\ \partial u_y / \partial y \\ \partial u_z / \partial z \\ (\partial u_y / \partial z) + (\partial u_z / \partial y) \\ (\partial u_x / \partial z) + (\partial u_z / \partial x) \\ (\partial u_x / \partial y) + (\partial u_y / \partial x) \end{bmatrix} \tag{2.15}$$

If we substitute equations (2.1) and (2.2) into equation (2.15) for propagation independent of the coordinate x, we get:

$$\left.\begin{aligned}
\sigma_{xx} &= \lambda\left(\frac{\partial^2\phi}{\partial y^2}+\frac{\partial^2\phi}{\partial z^2}\right)\\
\sigma_{yy} &= \lambda\left(\frac{\partial^2\phi}{\partial y^2}+\frac{\partial^2\phi}{\partial z^2}\right)+2\mu\left(\frac{\partial^2\phi}{\partial y^2}+\frac{\partial^2\psi}{\partial y\partial z}\right)\\
\sigma_{zz} &= \lambda\left(\frac{\partial^2\phi}{\partial y^2}+\frac{\partial^2\phi}{\partial z^2}\right)+2\mu\left(\frac{\partial^2\phi}{\partial z^2}-\frac{\partial^2\psi}{\partial y\partial z}\right)\\
\sigma_{yz} &= \sigma_{zy} = \mu\left(2\frac{\partial^2\phi}{\partial y\partial z}+\frac{\partial^2\psi}{\partial z^2}-\frac{\partial^2\psi}{\partial y^2}\right)\\
\sigma_{xz} &= \sigma_{zx} = \sigma_{xy} = \sigma_{yx} = 0
\end{aligned}\right\} \tag{2.16}$$

If we substitute equations (2.9) and (2.10) into equation (2.16) and look for solutions to surface waves by applying the stress free boundary condition at the surface $y = 0$, we get:

$$\left.\begin{aligned}
B &= \frac{2jk_R q}{k_R^2+s^2}A\\
A &= -\frac{2jk_R s}{k_R^2+s^2}B
\end{aligned}\right\} \tag{2.17}$$

Combining equations (2.11), (2.12), and (2.17), the Rayleigh wave characteristic equation can be found as:

$$\left(\frac{k_s^2}{k_R^2}-2\right)^4-16\left(1-\frac{k_l^2}{k_R^2}\right)\left(1-\frac{k_s^2}{k_R^2}\right)=0, \tag{2.18}$$

or,

$$\left(\frac{V_R^2}{V_s^2}-2\right)^4-16\left(1-\frac{V_R^2}{V_l^2}\right)\left(1-\frac{V_R^2}{V_s^2}\right)=0, \tag{2.19}$$

where V_R and k_R are the velocity and wave number of the Rayleigh wave, respectively.

To find a real value solution to equation (2.19), we express V_R in terms of V_s and Poisson's ratio, where Poisson's ratio is given by

$$\nu=\frac{(V_l/V_s)^2-2}{2\left[(V_l/V_s)^2-1\right]}. \tag{2.20}$$

Combining equations (2.19) and (2.20), it can be shown easily that

$$\nu=-\frac{\left(8(V_R/V_s)^2-16(V_R/V_s)^4+8(V_R/V_s)^6-(V_R/V_s)^8\right)}{8(V_R/V_s)^4-8(V_R/V_s)^6+(V_R/V_s)^8}. \tag{2.21}$$

It has been shown by I. A. Viktorov[4] that V_R can be found from the approximate form:

$$\frac{V_R}{V_s}\approx\frac{0.87+1.12\nu}{1+\nu}, \tag{2.22}$$

A more accurate result is given by curve fitting equation (2.21), the result is

$$\frac{V_R}{V_s}=0.87379+0.20178\nu-0.077453\nu^2 \tag{2.23}$$

Figure 2.2 shows a comparison of equations (2.22), (2.23) with the theoretical data generated from equation (2.21). Figure 2.3 shows the corresponding error from theoretical value (2.21) of equations (2.22) and (2.23).

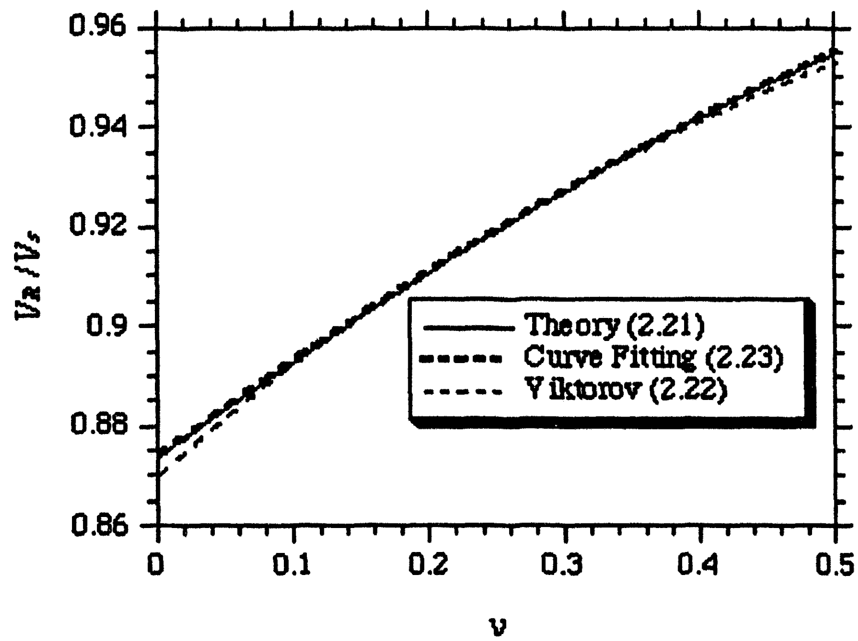

Figure 2.2 Rayleigh wave velocity V_R as a function of Poisson's ratio ν

As shown in Figure 2.2, the curve fitting result given by equation (2.23) fits the theoretical data given by equation (2.21) so well that it is difficult to distinguish them in the plot from one another. The approximate solution given by equation (2.22), though it generally agrees well with the exact solution, is not sufficiently accurate at both large and small Poisson's ratio region. Figure 2.3 shows that the curve fitting result (2.23) has an error which is generally smaller than 0.02 percent throughout the Poisson's ratio range from 0 to 0.5, while the largest error from equation (2.22) is 0.45 percent. For the case of ceramics, where $\nu \approx 0.2616$, theoretical value of V_R / V_s is 0.9212958, the approximate solution has a value of 0.9218384 with an error of -0.059 percent, while the curve fitting result has a value of 0.9212750 with an error of only 0.0024 percent.

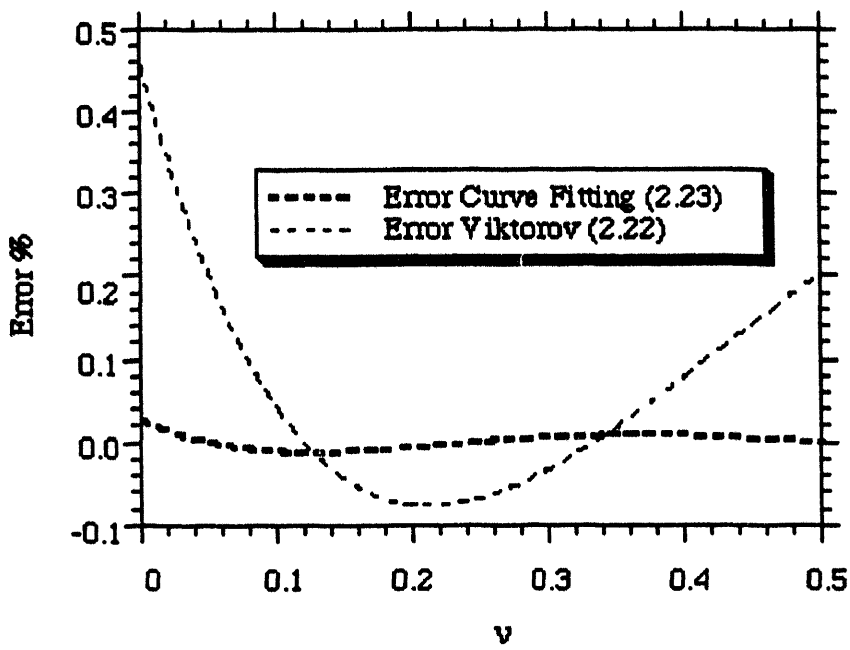

Figure 2.3 Error percentage comparison between equations (2.22) and (2.23)

As will be shown later in chapter 4, the laser-ultrasound technique is capable of measuring material acoustic velocities V_s and V_l to an accuracy of one in 10^4. To predict and compare the resonance frequencies of surface wave resonances on a sphere, we have to have an accurate value for the surface wave velocity V_R. Therefore it is necessary to use equation (2.23) in stead of equation (2.22) to calculate V_R.

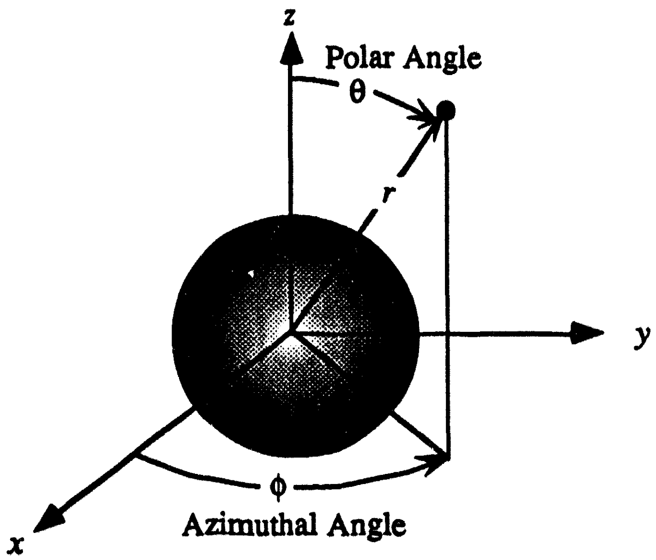

Figure 2.4 Definition of spherical coordination system

2.3 Resonance of Spheres

2.3.1 Basics

In the literature, there has been little research that deals with resonance of spheres, no matter whether it is experimental or theoretical. The papers by K. Sezawa[9] and by Yasuo Satô and Tatsuo Usami in 1962[10] are the fundamental towards the understanding of the frequencies and distribution of displacement of the free oscillations.

We use the following notation:

θ : polar angle

ϕ: azimuthal angle

r: coordinate in the radial direction (refer to figure 2.4 for θ, ϕ, and r)

a: Radius of sphere

f: Frequency

V_s: Shear wave velocity

V_l: Longitudinal wave velocity

k_s: Shear wave number

k_l: Longitudinal wave number

η: $2\pi fa / V_s = k_s a$

ξ: $2\pi fa / V_l = k_l a$

m: Integer, for variation in ϕ direction (will become clear later)

n: Integer, for variation in θ direction (will become clear later)

λ and μ: Lamé constants

$\boldsymbol{u} = \left(u_r, u_\theta, u_\phi\right)$: Mechanical displacement vector

$\boldsymbol{\sigma} = \left(\sigma_{rr}, \sigma_{r\theta}, \sigma_{r\phi}\right)$: Stress components on the surface of the sphere

A_{mn}, B_{mn}, C_{mn}: Arbitrary Constants

We express the radial, polar and azimuthal components of the displacement vector as $\boldsymbol{u} = \left(u_r, u_\theta, u_\phi\right)$. K. Sezawa derived solutions to the Helmholtz's equations (2.3) and

(2.4) in a spherical coordinate system. For solutions related to Φ in equation (2.3), the displacement vector is given by:

$$\left.\begin{aligned} u_{r,1} &= -\frac{A_{mn}}{k_l^2}\frac{d}{dr}\left(\frac{J_{n+1/2}(k_l r)}{r^{1/2}}\right)P_n^m(\cos\theta)\cos(m\phi) \\ u_{\theta,1} &= -\frac{A_{mn}}{k_l^2}\frac{J_{n+1/2}(k_l r)}{r^{3/2}}\frac{d}{d\theta}P_n^m(\cos\theta)\cos(m\phi) \\ u_{\phi,1} &= \frac{mA_{mn}}{k_l^2}\frac{J_{n+1/2}(k_l r)}{r^{3/2}}\frac{P_n^m(\cos\theta)}{\sin\theta}\sin(m\phi) \end{aligned}\right\} \tag{2.24}$$

There are two sets of solutions for Ψ in equation (2.4). The first set solves for the full solution, and the displacement vector is given by:

$$\left.\begin{aligned} u_{r,2} &= -\frac{n(n+1)B_{mn}}{k_s^2}\frac{J_{n+1/2}(k_s r)}{r^{3/2}}P_n^m(\cos\theta)\cos(m\phi) \\ u_{\theta,2} &= -\frac{B_{mn}}{k_s^2}\frac{1}{r}\frac{d}{dr}\left(r^{1/2}J_{n+1/2}(k_s r)\right)\frac{d}{d\theta}P_n^m(\cos\theta)\cos(m\phi) \\ u_{\phi,2} &= \frac{mB_{mn}}{k_s^2}\frac{1}{r}\frac{d}{dr}\left(r^{1/2}J_{n+1/2}(k_s r)\right)\frac{P_n^m(\cos\theta)}{\sin\theta}\sin(m\phi) \end{aligned}\right\} \tag{2.25}$$

The second set of solutions to equation (2.4) is for a pure torsional case where the radial component of Ψ is equal to zero, and the displacement vector is given by:

$$\left.\begin{aligned} u_{r,3} &= 0 \\ u_{\theta,3} &= \frac{mC_{mn}}{n(n+1))}\frac{J_{n+1/2}(k_s r)}{r^{1/2}}\frac{P_n^m(\cos\theta)}{\sin\theta}\cos(m\phi) \\ u_{\phi,3} &= -\frac{C_{mn}}{n(n+1)}\frac{J_{n+1/2}(k_s r)}{r^{1/2}}\frac{d}{d\theta}P_n^m(\cos\theta)\sin(m\phi) \end{aligned}\right\} \tag{2.26}$$

In equations (2.24), (2.25), and (2.26), the subscripts 1, 2, and 3 stand for three sets of solutions, namely solution to Φ, solution to Ψ, and solution to Ψ with no radial component. The term $J_{n+1/2}$ is the spherical Bessel function and $P_n^m(\cos\theta)$ is the associated Legendre function. As shown in the three sets of equations, n stands for variation in the θ direction. With $|m| \le n$, there are $2n+1$ degenerate modes that are represented by m in the ϕ direction.

The stress components corresponding to equations (2.24), (2.25), and (2.26) are given by Satô and Usami as shown in equations (2.27), (2.28), and (2.29), respectively:

$$\left.\begin{aligned}
\sigma_{rr,1} &= A_{mn}\left\{(\lambda+2\mu)\frac{J_{n+1/2}(k_l r)}{r^{1/2}}\right.\\
&\quad\left.+\frac{2\mu}{k_l^2}\left(\frac{2}{r}\frac{d}{dr}\left(\frac{J_{n+1/2}(k_l r)}{r^{1/2}}\right)-n(n+1)\frac{J_{n+1/2}(k_l r)}{r^{5/2}}\right)\right\}\\
&\quad\cdot P_n^m(\cos\theta)\cos(m\phi)\\
\sigma_{r\theta,1} &= -\frac{2\mu A_{mn}}{k_l^2}\frac{d}{dr}\left(\frac{J_{n+1/2}(k_l r)}{r^{3/2}}\right)\frac{d}{d\theta}P_n^m(\cos\theta)\cos(m\phi)\\
\sigma_{r\phi,1} &= \frac{2m\mu A_{mn}}{k_l^2}\frac{d}{dr}\left(\frac{J_{n+1/2}(k_l r)}{r^{3/2}}\right)\frac{P_n^m(\cos\theta)}{\sin\theta}\sin(m\phi)
\end{aligned}\right\} \quad (2.27)$$

$$\left.\begin{aligned}
\sigma_{rr,2} &= -\frac{2n(n+1)\mu B_{mn}}{k_s^2}\frac{d}{dr}\left(\frac{J_{n+1/2}(k_s r)}{r^{3/2}}\right)P_n^m(\cos\theta)\cos(m\phi) \\
\sigma_{r\theta,2} &= -\frac{\mu B_{mn}}{k_s^2}\left\{\frac{d^2}{dr^2}\left(\frac{J_{n+1/2}(k_s r)}{r^{1/2}}\right)+(n(n+1)-2)\frac{J_{n+1/2}(k_s r)}{r^{5/2}}\right\} \\
&\quad\cdot\frac{d}{d\theta}P_n^m(\cos\theta)\cos(m\phi) \\
\sigma_{r\phi,2} &= \frac{m\mu B_{mn}}{k_s^2}\left\{\frac{d^2}{dr^2}\left(\frac{J_{n+1/2}(k_s r)}{r^{1/2}}\right)+(n(n+1)-2)\frac{J_{n+1/2}(k_s r)}{r^{5/2}}\right\} \\
&\quad\cdot\frac{P_n^m(\cos\theta)}{\sin\theta}\sin(m\phi)
\end{aligned}\right\} \tag{2.28}$$

$$\left.\begin{aligned}
\sigma_{rr,3} &= 0 \\
\sigma_{r\theta,3} &= \frac{m\mu C_{mn}}{n(n+1)}\left\{\frac{d}{dr}\left(\frac{J_{n+1/2}(k_s r)}{r^{1/2}}-\frac{J_{n+1/2}(k_s r)}{r^{3/2}}\right)\right\} \\
&\quad\cdot\frac{P_n^m(\cos\theta)}{\sin\theta}\cos(m\phi) \\
\sigma_{r\phi,3} &= -\frac{\mu C_{mn}}{n(n+1)}\left\{\frac{d}{dr}\left(\frac{J_{n+1/2}(k_s r)}{r^{1/2}}-\frac{J_{n+1/2}(k_s r)}{r^{3/2}}\right)\right\} \\
&\quad\cdot\frac{d}{d\theta}P_n^m(\cos\theta)\sin(m\phi)
\end{aligned}\right\} \tag{2.29}$$

If we look for solutions for the free resonance of a sphere with the boundary condition that requires no normal stress on the spherical surface, Satô and Usami have shown that the above three equations can be combined into two groups. The first group is formed by a combination of longitudinal and shear waves, coming from equations (2.27) and (2.28), this is called the spheroidal mode. The second group is a pure torsional case coming from equation (2.29). In the following two sections, we are going to discuss in more detail these two groups of resonances.

2.3.2 Torsional Resonance of a Homogeneous Elastic Sphere ($T_{nlm} \rightarrow T_{nl}$)

Equation (2.29) pertains to pure torsional resonance modes. In this case, there is no radial component of the displacement vector. The first sub-index n stands for variation in the polar angle θ direction. The second sub-index l stands for the l^{th} harmonic of the n^{th} resonance, where l = 1, 2, ..., ∞. For each n, there are $(2n+1)$ degenerate modes in the azimuthal ϕ direction represented by m, where $|m| \leq n$. These degenerate modes have the same resonant frequencies; therefore, the T_{nlm} modes can be represented by T_{nl} modes. The characteristic equation is deduced from the boundary conditions on the surface, that is,

$$\left.\begin{aligned} \sigma_{r\theta}\big|_{r=a} &= 0 \\ \sigma_{r\phi}\big|_{r=a} &= 0 \end{aligned}\right\}, \tag{2.30}$$

where a is the radius of the sphere. If we substitute equation (2.30) into (2.29), we get two solutions of the same form given by:

$$\frac{d}{d\eta}\left(\frac{J_{n+1/2}(\eta)}{\eta^{3/2}}\right) = 0 \tag{2.31}$$

where $\eta = k_s a = \dfrac{\omega a}{V_s}$, this equation reduces to

$$(n-1)J_{n+1/2}(\eta) - \eta J_{n+3/2}(\eta) = 0 \tag{2.32}$$

As shown in equation (2.32), the resonant frequencies of the torsional resonances are dependent upon the radius of the sphere a and the shear wave velocity V_s only. Figure 2.5 shows an example of one of the torsional modes T_{11} mode for Si_3N_4 ceramic bearing with V_s = 6250m/sec. In this figure we assume m = 0, therefore $u_\theta = 0$ according equation (2.26), and only u_ϕ is non-zero. The picture on the left is a 3-D plot of u_ϕ versus r and q, the displacement is normalized according to the largest value, and radius of the sphere is assumed to be one. The picture on the right illustrates that this is a case of a rigid rotation with two spherical shells moving in the shearing direction against each other[11].

2.3.3 Spheroidal Resonance of a Homogeneous Elastic Sphere ($S_{nlm} \rightarrow S_{nl}$)

Similarly to the torsional resonance case, the first sub-index n stands for variation in the polar angle θ. The second sub-index l stands for the l^{th} harmonic of

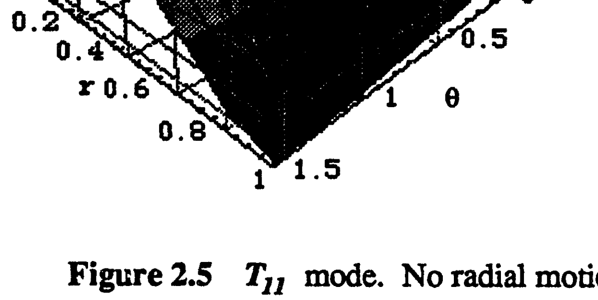

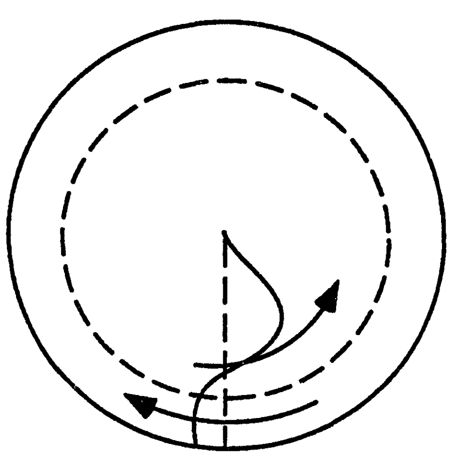

Figure 2.5 T_{11} mode. No radial motion, two spherical shells move in the shear direction against each other.

the n^{th} resonance, where $l = 1, 2, \ldots, \infty$. For each n, there are $(2n+1)$ degenerate modes in the azimuthal direction represented by m, where $|m| \leq n$. These degenerate modes have the same resonant frequency, therefore, the S_{nlm} modes can be represented by S_{nl} modes.

The treatment of the spheroidal resonances is much more complicated than the pure torsional resonances. Because of the excitation scheme used in our experiments, we can only consider the solutions for which the motion is independent of the azimuthal direction, i.e., $m = 0$. We can rewrite expressions (2.24) and (2.25) as:

$$\left.\begin{aligned} u_{r,1} &= -\frac{A_n}{k_l^2}\frac{d}{dr}\left(\frac{J_{n+1/2}(k_l r)}{r^{1/2}}\right)P_n(\cos\theta) \\ u_{\theta,1} &= -\frac{A_n}{k_l^2}\frac{J_{n+1/2}(k_l r)}{r^{3/2}}\frac{d}{d\theta}P_n(\cos\theta) \\ u_{\phi,1} &= 0 \end{aligned}\right\} \tag{2.33}$$

and

$$\left.\begin{aligned} u_{r,2} &= -\frac{n(n+1)B_n}{k_s^2}\frac{J_{n+1/2}(k_s r)}{r^{3/2}}P_n(\cos\theta) \\ u_{\theta,2} &= -\frac{B_n}{k_s^2}\frac{1}{r}\frac{d}{dr}\left(r^{1/2}J_{n+1/2}(k_s r)\right)\frac{d}{d\theta}P_n(\cos\theta) \\ u_{\phi,2} &= 0 \end{aligned}\right\} \tag{2.34}$$

Equations (2.27) and (2.28) become:

$$\left.\begin{aligned}
\sigma_{rr,1} &= A_n\left\{(\lambda+2\mu)\frac{J_{n+1/2}(k_l r)}{r^{1/2}}\right.\\
&\qquad \left.+\frac{2\mu}{k_l^2}\left(\frac{2}{r}\frac{d}{dr}\left(\frac{J_{n+1/2}(k_l r)}{r^{1/2}}\right)-n(n+1)\frac{J_{n+1/2}(k_l r)}{r^{5/2}}\right)\right\}P_n(cos\theta)\\
\sigma_{r\theta,1} &= -\frac{2\mu A_n}{k_l^2}\frac{d}{dr}\left(\frac{J_{n+1/2}(k_l r)}{r^{3/2}}\right)\frac{d}{d\theta}P_n(cos\theta)\\
\sigma_{r\phi,1} &= 0
\end{aligned}\right\} \tag{2.35}$$

and

$$\left.\begin{aligned}
\sigma_{rr,2} &= -\frac{2n(n+1)\mu B_n}{k_s^2}\frac{d}{dr}\left(\frac{J_{n+1/2}(k_s r)}{r^{3/2}}\right)P_n(cos\theta)\\
\sigma_{r\theta,2} &= -\frac{\mu B_n}{k_s^2}\left\{\frac{d^2}{dr^2}\left(\frac{J_{n+1/2}(k_s r)}{r^{1/2}}\right)+(n(n+1)-2)\frac{J_{n+1/2}(k_s r)}{r^{5/2}}\right\}\frac{d}{d\theta}P_n(cos\theta)\\
\sigma_{r\phi,2} &= 0
\end{aligned}\right\} \tag{2.36}$$

Sezawa has shown that under the condition

$$\begin{aligned}
\frac{B_n}{A_n} = \frac{k_s^2}{2k_l^2}\frac{d}{dr}\left(\frac{J_{n+1/2}(k_l r)}{r^{3/2}}\right)_{r=a}&\left[\frac{1}{\sqrt{r}}\frac{d^2}{dr^2}(J_{n+1/2}(k_s r))-\right.\\
&\left.\frac{1}{r^{3/2}}\frac{d}{dr}(J_{n+1/2}(k_s r))+\frac{1}{r^{5/2}}\left(n(n+1)-\frac{5}{4}\right)J_{n+1/2}(k_s r)\right]_{r=a}^{-1}
\end{aligned} \tag{2.37}$$

A summation of equation (2.35) and equation (2.36) satisfies the stress free boundary condition.

$$\left.\begin{aligned}
\sigma_{r\theta}\big|_{r=a} &= 0\\
\sigma_{r\theta}\big|_{r=a} &= 0
\end{aligned}\right\} \tag{2.38}$$

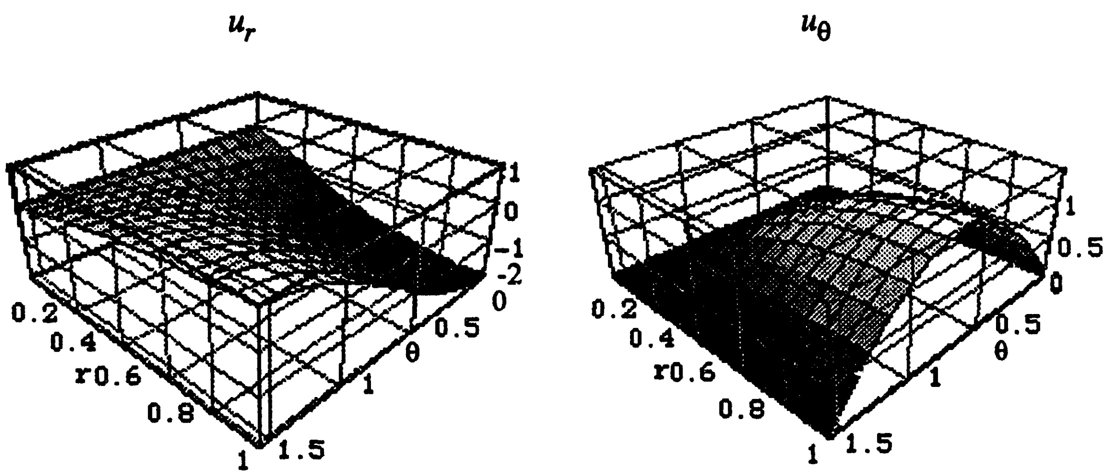

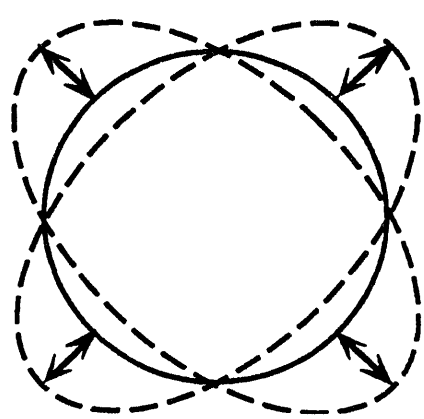

Figure 2.6 An example of the spheroidal S_{20} mode, also called the oblate-prolate mode.

The characteristic equation of the spheroidal resonance is then obtained as:

$$\frac{2k_l}{k_s}\left[\frac{1}{\eta}+\frac{(n-1)(n+2)}{\eta^2}\left(\frac{J_{n+3/2}(\eta)}{J_{n+1/2}(\eta)}-\frac{n+1}{\eta}\right)\right]\frac{J_{n+3/2}(\xi)}{J_{n+1/2}(\xi)}$$
$$+\left[-\frac{1}{2}+\frac{(n-1)(n+2)}{\eta^2}+\left(\frac{1}{\eta}-\frac{2n(n-1)(n+2)}{\eta^3}\right)\frac{J_{n+3/2}(\eta)}{J_{n+1/2}(\eta)}\right]=0 \tag{2.39}$$

where

$$\left.\begin{array}{l}\xi = k_l a \\ \eta = k_s a\end{array}\right\} \tag{2.40}$$

Equation (2.37) gives us the relative amplitude contribution for spheroidal resonance between shear wave and longitudinal wave. Equation (2.39) tells us that the resonance frequencies of the spheroidal modes, unlike the torsional modes, depend on V_l, V_s, and a, since they are combinations of longitudinal and shear wave components.

Figure 2.6 demonstrates an example of the spheroidal modes, in this case, the S_{20} mode for Si_3N_4 ceramic bearing ball with $V_s = 6250$m/s, $V_l = 11000$m/s. B_2/A_2 is calculated to be 0.281183 from equation (2.37), this is also called the oblate-prolate mode and is the fundamental spheroidal mode. The top two pictures are 3-D plots of displacements u_r and u_θ versus coordinates r and θ. The displacements are calculated according to $u_r = u_{r,1} + (B_2/A_2)\,u_{r,2}$ and $u_\theta = u_{\theta,1} + (B_2/A_2)\,u_{\theta,2}$. The amplitudes of the displacements are normalized with the maximum amplitude of u_r, and the radius of the sphere is assumed to be unity.

A special case of the spheroidal mode is the <u>pure compressional mode</u>. In this case $n = 0$ (implying $m = 0$, since $|m| \le n$), this means there is no variation in either θ or ϕ direction. There is displacement in the radial direction only. Equation (2.39) can be simplified to be:

$$tan(\xi) = \frac{\xi}{1 - \frac{1}{4}\eta^2} \tag{2.41}$$

where

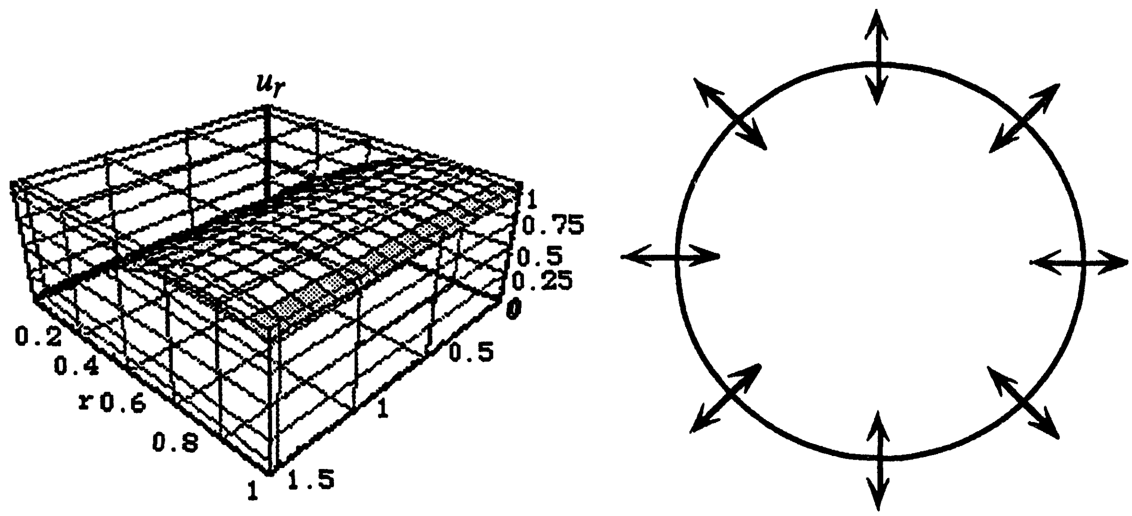

Figure 2.7 The S_{01} mode, the fundamental compressional mode, is also called the breathing mode. The entire sphere expands and contracts in unison.

$$\left.\begin{aligned} \xi &= k_l a \\ \eta &= k_s a \end{aligned}\right\} \tag{2.40}$$

The only non-zero displacement component in equations (2.24) and (2.25) is $u_{r,1}$. Figure 2.7 shows an example of the fundamental pure compressional mode, the S_{01} mode, also called the breathing mode. The entire sphere is observed to expand and contract in unison. For higher order pure compressional modes, there are different spherical shells moving against one another in the radial direction.

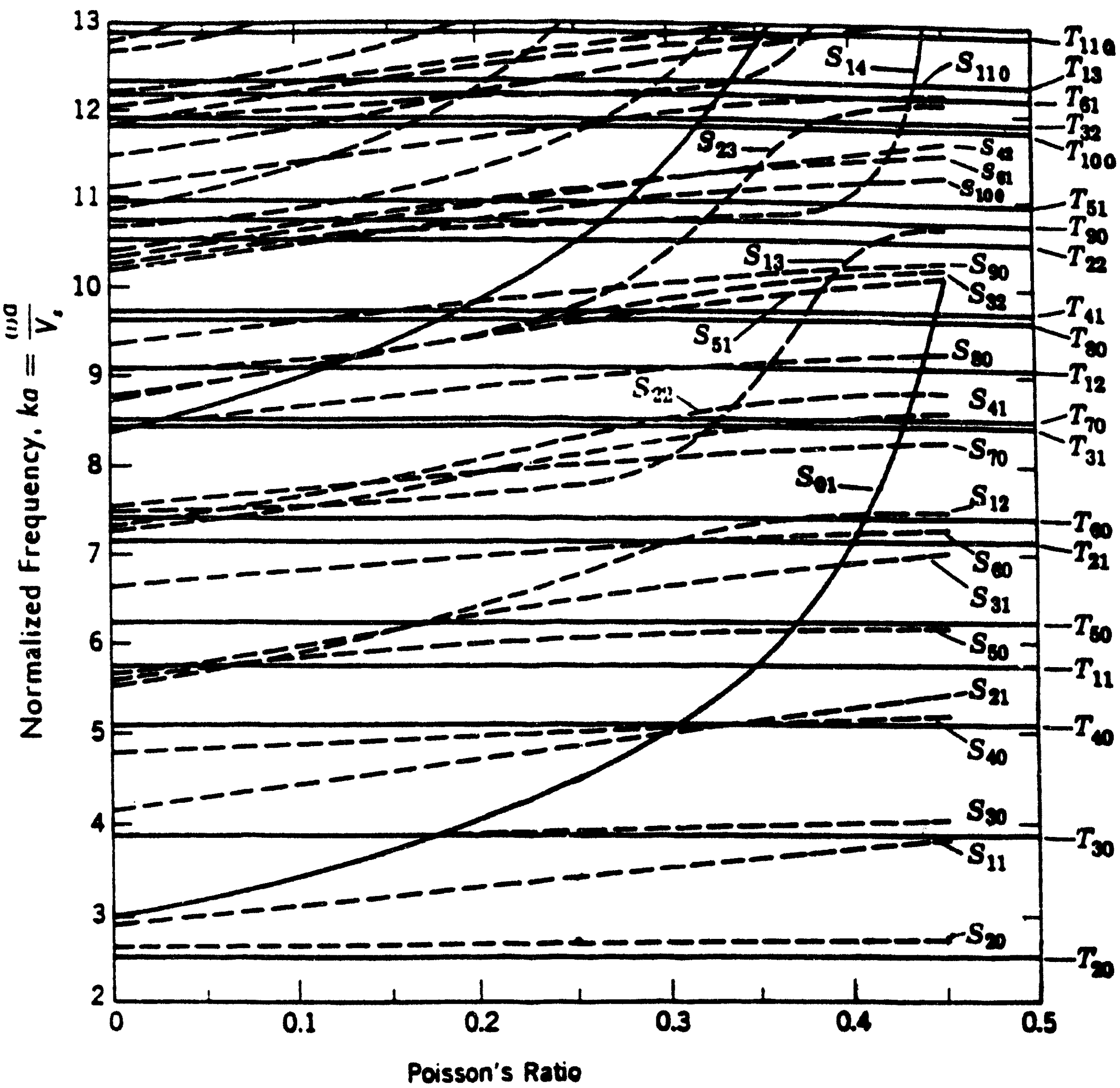

Figure 2.8 Mode chart for an isotropic spherical resonator of radius a, with stress-free boundary condition. The horizontal axis is Poisson's ratio $\nu = \left[(V_l/V_s)^2 - 2\right] / \left\{2\left[(V_l/V_s)^2 - 1\right]\right\}$. The vertical axis is normalized frequency. As can be seen from the chart, resonant frequencies of the torsional resonances are independent of V_l.

Figure 2.8 shows a low frequency mode chart of the free oscillation of a sphere[11]. As seen in the figure, the horizontal straight lines are the torsional resonances. These resonant frequencies of the torsional modes depend on the shear wave velocity V_s but not on the longitudinal wave velocity V_l. The spheroidal resonance frequencies, on the other hand, depend on both V_s and V_l.

2.3.4 Surface Acoustic Wave Resonance of a Homogeneous Elastic Sphere

For large values of n (n ≥ 100), we substitute an asymptotic expansion to the Bessel functions in the characteristic equation (2.39) and simplify it to the following form[12]:

$$\left(\frac{k_s^2}{k_R^2}-2\right)^4 - 16\left(1-\frac{k_l^2}{k_R^2}\right)\left(1-\frac{k_s^2}{k_R^2}\right)=0 \tag{2.42}$$

Equation (2.42) is the characteristic equation of Rayleigh waves, where k_R is the wave number of the Rayleigh waves. This tells us that Rayleigh waves exist on spherical surface at high frequencies.

2.3.5 SAW Propagation On A Sphere

As discussed in chapter 1, in the field of ultrasonics, surface wave probing is a good tool for surface defect inspection. However, to excite and detect surface waves on a sphere, we need to know how surface waves propagate on its surface. We have shown in the previous section the existence of surface wave resonances on a sphere. In this section, we use Green's function formalism, i.e., consider excitation at a point, to analyze the propagation of surface waves on a sphere[6]. We will show that surface waves excited at a point on one pole of a sphere are focused at the opposite pole of the sphere. This focusing effect assists us in the design of the experimental setups in chapters 3 and 4, where we use a point source to excite surface waves on a sphere, and detect at a point on the opposite side of the sphere.

Consider wave propagation on a spherical surface in the spherical coordinate system (r, θ, ϕ). With azimuthal symmetry, no radial dependence, and only θ as the independent coordinate variable, Helmholtz's equation reduces to:

$$\frac{1}{\sin\theta}\frac{d}{d\theta}\left(\sin\theta\frac{dH}{d\theta}\right)+k_R^2a^2H=0 \tag{2.43}$$

where H is a displacement potential, it can be either Φ or Ψ, or a linear combination thereof. Also, k_R is the wave number of the surface wave, and a is the radius of the sphere. Compare equation (2.43) to Legendre's equation[7]:

$$\frac{1}{\sin\theta}\frac{d}{d\theta}\left(\sin\theta\frac{dZ_\gamma(\cos\theta)}{d\theta}\right)+\gamma(\gamma+1)Z_\gamma(\cos\theta)=0 \tag{2.44}$$

As discussed in the previous section, Rayleigh waves on a spherical surface exist only at high frequencies. For $k_Ra>>1$, let

$$k_R^2a^2=\gamma(\gamma+1) \tag{2.45}$$

then

$$\gamma \approx k_R a - \frac{1}{2} \tag{2.46}$$

The solution to equation (2.44) can be chosen to be[13]:

$$Z_\gamma(\cos\theta) = Q_\gamma(\cos\theta) - jP_\gamma(\cos\theta) \tag{2.47}$$

where $Q_\gamma(\cos\theta)$ and $P_\gamma(\cos\theta)$ are Legendre Polynomials of the second kind and first kind, respectively. The sign of the imaginary part is chosen to give an asymptotic form equivalent in this context to surface wave propagation in one direction along a plane semi-infinite substrate.

We use Green's function formalism to obtain the field distribution of surface waves on a sphere. To solve for the Green's function $G(\theta)$ of surface wave potential on a sphere, some properties of Legendre polynomials have to be understood. The first one is the recurrence relation given by[7]:

$$\left(x^2 - 1\right)\frac{d}{dx}Z_\gamma(x) = (\gamma+1)Z_{\gamma+1}(x) - (\gamma+1)xZ_\gamma(x) \tag{2.48}$$

Second, it can be shown by mathematical induction that:

$$\lim_{x\to 1}(\gamma+1)\left[Q_{\gamma+1}(x) - xQ_\gamma(x)\right] = -1 \tag{2.49}$$

To find the two dimensional Green's function $G(\theta)$ corresponding to the potential Φ or Ψ satisfying the wave equation:

$$\nabla^2 G + k_R^2 G = \delta(\theta) \tag{2.50}$$

where ∇^2 corresponds to differentiation only in the θ direction, where $\delta(\theta)$ is the Dirac delta function, which satisfies the equation

$$\oiint \delta(\theta)\, d\boldsymbol{\Omega} = 1 \tag{2.51}$$

with $\delta(\theta) \rightarrow \infty$ as $\theta \rightarrow 0$, and where

$$d\boldsymbol{\Omega} = 2\pi a^2 \sin\theta\, d\theta \tag{2.52}$$

We write the solution to equation (2.50) as

$$G(\theta) = A\left[Q_\gamma(\cos\theta) - j P_\gamma(\cos\theta)\right] \tag{2.53}$$

To find the constant A, we integrate equation (2.50) over a small spherical surface element enclosing the point $\theta = 0$. Thus

$$\lim_{\theta \to 0} \oiint \left(\nabla^2 G + (k_R a)^2 G\right) d\boldsymbol{\Omega} = 1 \tag{2.54}$$

Combining equations (2.51), (2.52), (2.53), (2.54), plus an application of Gauss's theorem gives:

$$\lim_{\theta \to 0}\left[\int_0^\theta k_R^2 G \cdot \left(2\pi a^2 \sin\theta\right) d\theta + \int_{\phi=0}^{2\pi} \frac{dG}{d\theta} \sin\theta\, d\phi\right] = 1 \tag{2.55}$$

Substituting (2.53) into (2.55), using the relationship given by (2.48) and (2.49), and solving for A in equation (2.53), we get:

$$G(\theta) = \frac{-1}{2\pi}\left[Q_\gamma(\cos\theta) - j P_\gamma(\cos\theta)\right] \tag{2.56}$$

For $\gamma >> 1$ and θ sufficiently larger than zero, the asymptotic solutions of the Legendre Polynomials are:

$$P_\gamma(\cos\theta) \approx \left(\frac{\pi}{2\gamma \sin\theta}\right)^{1/2} \sin\left[\left(\gamma+\frac{1}{2}\right)\theta+\frac{\pi}{4}\right] \tag{2.57}$$

$$Q_\gamma(\cos\theta) \approx \left(\frac{\pi}{2\gamma \sin\theta}\right)^{1/2} \cos\left[\left(\gamma+\frac{1}{2}\right)\theta+\frac{\pi}{4}\right] \tag{2.58}$$

Substituting (2.46), (2.57), and (2.58) into (2.56), we have

$$G(\theta) \approx -\left(\frac{1}{8\pi\left(k_R a-\frac{1}{2}\right)\sin\theta}\right)^{1/2} \exp\left[-j\left(k_R a\theta+\frac{\pi}{4}\right)\right] \tag{2.59}$$

Equation (2.59) is a very important result. It contains physical meaning in its structure. First, the $-jk_R a\theta$ term inside the exponential describes propagation of a

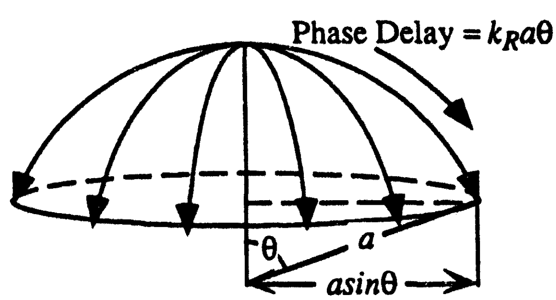

Figure 2.9 This figure illustrates two physical phenomena in equation (2.50). (i) Polar angle propagation. (ii) Cylindrical wave attenuation.

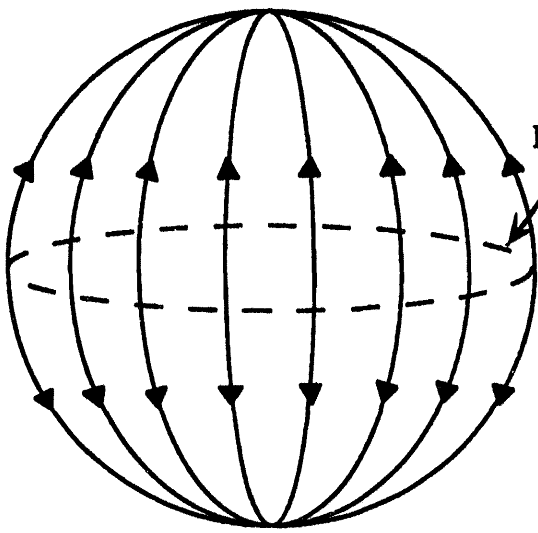

Figure 2.10 Focusing effect of surface acoustic waves on a sphere.

Rayleigh wave in the polar angle θ direction, with a phase delay of $k_R a\theta$, as shown in Figure 2.9. This explains the reason for the negative sign in equation (2.47). Second, the $a sin\theta$ term in the denominator of the square root corresponds to the decrease in amplitude of a cylindrical wave as its area increases. The amplitude reduction of a cylindrical wave is proportional to $1/\sqrt{\text{radius}}$. For a surface acoustic wave propagating on the surface of a sphere, the circumference is equal to $2\pi\, a\, sin\theta$, as shown also in Figure 2.9.

(2.59), this is a singular point because of the $sin\theta$ term in the denominator. Therefore, the field near the focal point needs further treatment. Refer to figure 2.11, in actual experiments, there is no so called 'point source', the excitation actually takes place over an area of finite size, and the focal point will not be exactly be an angle of π away from the source. We understand that the field distribution should be independent of the azimuthal direction because of our excitation scheme. To calculate the field distribution near the south pole, we can arbitrarily put a ring-type source at any polar angle sufficiently away from the two poles and perform Green's function integration over the source. Readers interested in the integration procedure are referred to chapter 3 of Professor G. S. Kino's book '*Acoustic Waves: Devices, Imaging, and Analog Signal Processing*.'[6] We chose the equator as the ring-type source and calculated the field distribution $H(\theta)$ near the south pole by integrating the Green's function over source using the Kirchhoff formula in Kino's book:

$$H(\theta,\phi) \equiv H(\theta) = \int_s \left(H\nabla' G(\vartheta) - G(\vartheta)\nabla' H\right)\cdot \boldsymbol{n}\, ds \tag{2.60}$$

where ds is an element of the ring-type source, $\boldsymbol{n}$ is a normal vector pointing in the negative θ direction, s is the entire ring of the source (integration from 0 to 2π).

There is a reason why we chose the equator as the source. Kino pointed out that it is not rigorously correct to specify both H and $\nabla' H$ on the source, however, since the length of the equator is much larger than the wave length, we can assume $\nabla' H \cdot \boldsymbol{n} = jk_R H$ in the equation.

Referring to figure 2.11, the angle ϑ is the angle extended on the spherical surface between a point on the source (a,θ_0,ϕ_0) and the point (a,θ,ϕ) of which the field we are interested in, ϑ is given by:

$$\vartheta = cos^{-1}\left[sin\theta\, sin\theta_0\, cos(\phi-\phi_0)+cos\theta\, cos\theta_0\right] \tag{2.61}$$

Note in the case of using the equator as the source, $\theta_0 = \pi/2$. The integration result is shown in figure 2.12. In this figure, the vertical axis is normalized with the amplitude at the focal point, the horizontal axis is distance away from the focal point and is normalized with surface wavelength.

We observe that surface waves are focused at the south pole of the sphere. At a distance λ_R away from the focal point, the normalized amplitude drops to $1/\sqrt{2}$, therefore we say the 3dB spot size is two times this distance, or, $0.364\lambda_R$. The observation of the focusing phenomenon is important for experimental purposes, it tells us that in order to detect the highest amplitude to have the largest signal to noise ratio, the detection point has to be either at the excitation point, or at the opposite pole, in our case, the south pole.

Finally, to form a surface wave resonance, the sphere's circumference must be an integral number of surface wavelengths, given by the formula:

$$\frac{2\pi a}{\lambda_R} = \mathrm{M}-1 \tag{2.62}$$

where M is an integer.

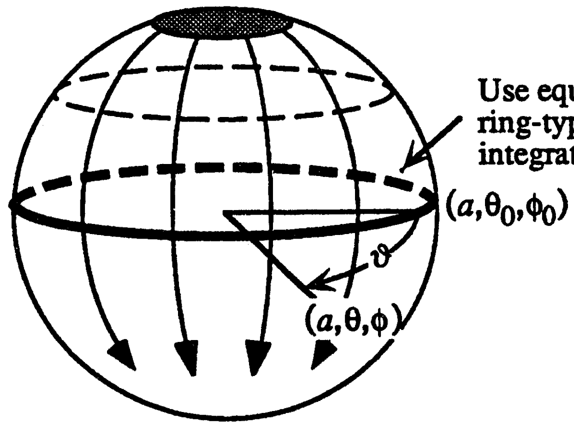

Figure 2.11 Treat surface wave source with a finite dimension in stead of a point source

The physical meaning is that as surface wave travels, its phase encounters a change of $k_R(\pi a)$ after the first half circumference with a traveling distance of πa, π after the first focal point, another $k_R(\pi a)$ after the second half circumference, another π after it refocused at the source. Thus after traveling one round-trip we have a total phase change of:

$$[2k_R(\pi a)+2\pi]=[2\pi(1+k_R a)]=[2\pi(1+2\pi a/\lambda_R)] \tag{2.63}$$

In order to form a resonance, this sum should be an integer number of 2π. Therefore, $1+2\pi a/\lambda_R = \mathrm{M}$, this gives the result in (2.60).

We have used Green's function integration to calculate field distribution on the sphere. Here we will show a much simpler approach with a lot more physical meaning. The Green's function for a traveling wave was given by

$$G(\theta)=\frac{-1}{2\pi}\left[Q_\gamma(\cos\theta)-jP_\gamma(\cos\theta)\right] \tag{2.56}$$

To form standing waves, there is another Green's function for waves traveling in the opposite direction, namely:

$$G'(\theta)=\frac{-1}{2\pi}\left[Q_\gamma(\cos\theta)+jP_\gamma(\cos\theta)\right] \tag{2.56'}$$

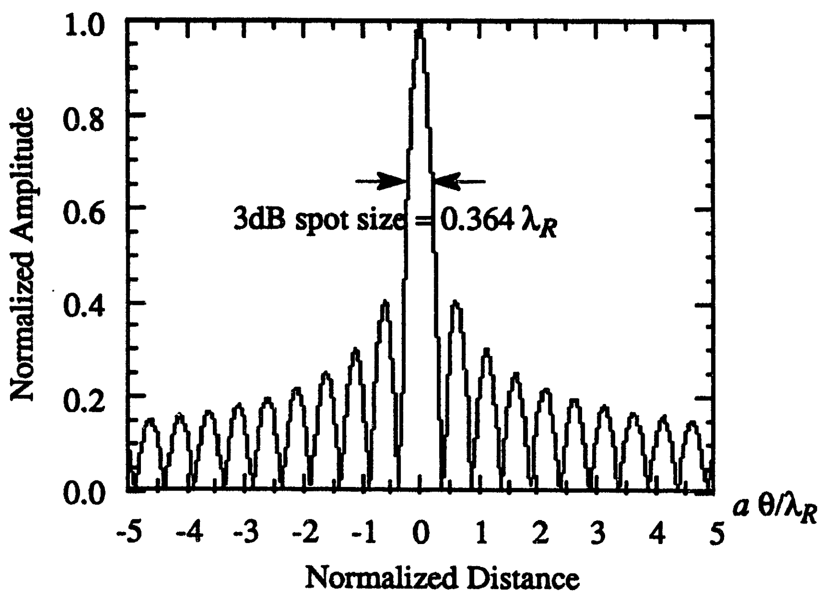

Figure 2.12 Standing wave pattern of surface waves on a sphere. Here, the horizontal axis is normalized with respect to surface wavelength λ_R. We see that surface waves focus down to a $0.364\ \lambda_R$ 3-dB spot size.

Therefore, the standing wave pattern is actually $(G+G')$ and is proportional to $Q_\gamma(cos\theta)=Q_{k_Ra-1/2}(cos\theta)=Q_{M-3/2}(cos\theta)$, where M is an integer. When this expression is plotted against figure 2.12, they are found to be identical.

2.4 Concluding Remarks

In this chapter, we discussed briefly the propagation of Rayleigh waves on a planar surface. Further, we discussed in more detail about the theories of spherical resonances. The torsional resonance frequencies are found to be dependent on the shear wave velocity and radius of the sphere, while the spheroidal resonance frequencies are dependent on the shear wave velocity, the longitudinal wave velocity, and radius of the sphere.

Surface wave resonances are found to be one of the special cases of the spheroidal resonances. We used Green's function approach to show the focusing effect of surface waves propagating on a sphere. The focal point spot size is found to be $0.364\lambda_R$. This enables us to design the excitation and detection scheme for surface waves to be used in Chapters 3 and 4.

REFERENCES

[1] Lord Rayleigh, *On Waves Propagated Along the Plane Surfaces of an Elastic Solid*, Proc. London Math. Soc., **17**, 4-11 (1885).

[2] J. J. Tien, *Surface Acoustic Wave Probing of Ceramics*, Ph.D. dissertation, Stanford University, 1983.

[3] M. T. Resch, *Non-Destructive Evaluation of Small Surface Cracks Using Surface Acoustic Waves*, Ph. D. dissertation, Stanford University, 1982.

[4] I. A. Viktorov, *Rayleigh and Lamb Waves*, Plenum Press, New York (1967).

[5] Lord Rayleigh, *On Waves Propagated Along the Plane Surfaces of an Elastic Solid*, Proc. London Math. Soc., **17**, 4-11 (1885).

[6] G. S. Kino, *Acoustic Waves: Devices, Imaging, and Analog Signal Processing* Prentice-Hall, New Jersey, (1987).

[7] George Arfken, *Mathematical Methods for Physicists*, 3rd edition, Academic Press, INC., Florida (1985).

[8] B. A. Auld, *Acoustic Fields and Waves in Solids*, **I**, Wiley, New York (1973).

[9] K. Sezawa, *Dilatational and Distortional Waves Generated from a Cylindrical or a Spherical Origin*, Bull. Earthq. Res. Inst., **2** (1924).

[10] Yasuo Satô and Tatsuo Usami, Geophys. Mag. **31**, 25 (1962).

[11] B. A. Auld, *Acoustic Fields and Waves in Solids*, **II**, Wiley, New York (1973).

[12] K. Sezawa, *On the Propagation of Rayleigh Waves on Plane and Spherical Surfaces*, Bull. Earthq. Res. Inst., **2** (1924).

[13] C. P. Hsieh, C-H Chou, and B. T. Khuri-Yakub, *Surface Acoustic Wave Probing of Ceramic Bearing Balls*, in *Review of Progress in Quantitative Nondestructive Evaluation,* Eds. D. O. Thompson and D. E. Chimenti (Plenum Press, New York, 1990).

Chapter 3

Contact-Contact Resonant Sphere Technique

3.1 Introduction

The resonant sphere technique was originally introduced by D. B. Fraser and L. C. LeCraw in 1964 as a technique to measure material properties of spherical objects[1]. A sphere was put on a piezoelectric transducer, and surrounded by cardboard to prevent it from rolling. A tone burst signal was sent into the transducer and the gated reflected signal was detected using the same transducer. Resonance frequency was determined when the maximum reflection amplitude was found. The quality factor of each resonance was determined by measuring the decay rate of the reflected signal. This proved to be a useful technique for measuring acoustic properties such as longitudinal wave velocity V_l and shear wave velocity V_s. Several researchers continued on with this technique, but all limited its usage to measuring material properties[2,3].

In chapter 2 we discussed wave propagation on spheres. Waves propagating in opposite directions on the sphere will form standing waves. At certain frequencies, these standing waves will form resonances on the sphere. Researchers following in the footsteps of Fraser used the resonant sphere technique in the low frequency region to measure material properties. In this chapter, we will present our improvements and modifications of this technique. First, we improved the experimental setup to enable the system to measure not only the resonance amplitude but also its phase. Second, we pushed the operation to a high frequency region and, for the first time, experimentally demonstrated surface wave resonances on spheres. Since we are able to generate surface waves on spheres, these surface waves can be used to perform surface defect inspection, particularly of ceramic bearing balls which are of most interest to this research.

3.2 Experimental Setup

We designed and built a contact-contact resonance experimental setup to measure resonances of spheres. The setup is shown in Figure 3.1. The sphere is mechanically mounted between two $LiNbO_3$ longitudinal transducers. The signal from the first synthesizer is inserted into the bottom transducer (transducer 1), on which the ball rests, and excites continuous ultrasonic waves on the sphere, in this case, a ceramic bearing ball. The top transducer, which is similar to the bottom transducer, acts as a receiver. It is positioned to make a light contact with the sphere. To detect both the phase and amplitude of the acoustic resonance signal which depend on the displacement of the north pole of the sphere, the received signal is mixed with a signal from the second synthesizer with a frequency setting which is 5 KHz lower than that of the first synthesizer. After mixing, the signal is sent into a lock-in amplifier. Signals from the trigger output channels of both synthesizers are also mixed, low pass filtered at 5 KHz, and then sent into the reference channel of the lock-in amplifier. We designed a computer-controlled system to sweep over the frequency range of interest at a fixed, but arbitrary, frequency increment. Local maxima in amplitude are used to determine the resonance frequencies of the sphere, whereas the phase of the spectrum is used to measure the resonance Q's[4].

Before each measurement, we had to make sure that the static force between the transducers and the sphere was as light as possible. To achieve this goal, the position of the top transducer was controlled by an x - y - z stage, with the spring connecting the stage and the transducer. Once a signal was observed, we gradually lifted the position of the top transducer. When a sudden disappearance of signal was found, the position of the top transducer was lowered by a very small distance, usually this meant a quarter turn of

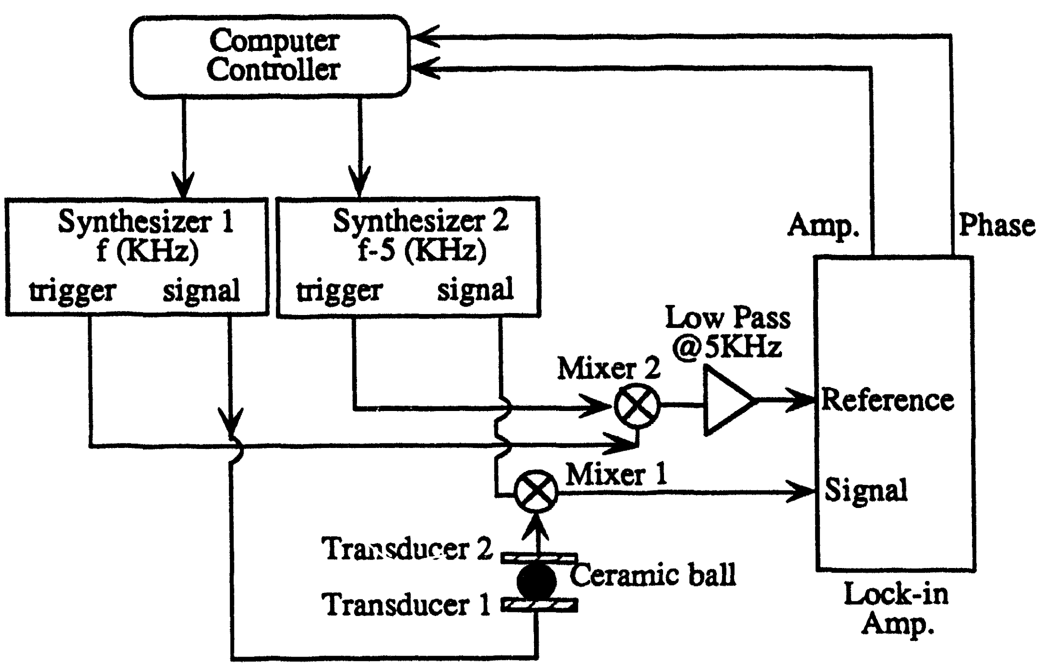

Figure 3.1 Contact-contact spherical resonance experiment setup

the stage knob, which corresponds to a compression in the spring of the order of 10 μm.

Figure 3.2 shows a detailed diagram of the transducer-sphere configuration. As shown in the figure, the two transducers are mounted on two springs. The purpose of having two springs is to insure that the transducers are in light contact with the sphere, and the free oscillation condition of the sphere can be closely simulated.

3.3 Signal Processing Analysis

The mathematics behind the analog signal processing scheme shown in Figure 3.1 can be explained in more detail as follows. The output from both the signal and the trigger channels of synthesizer 1 is:

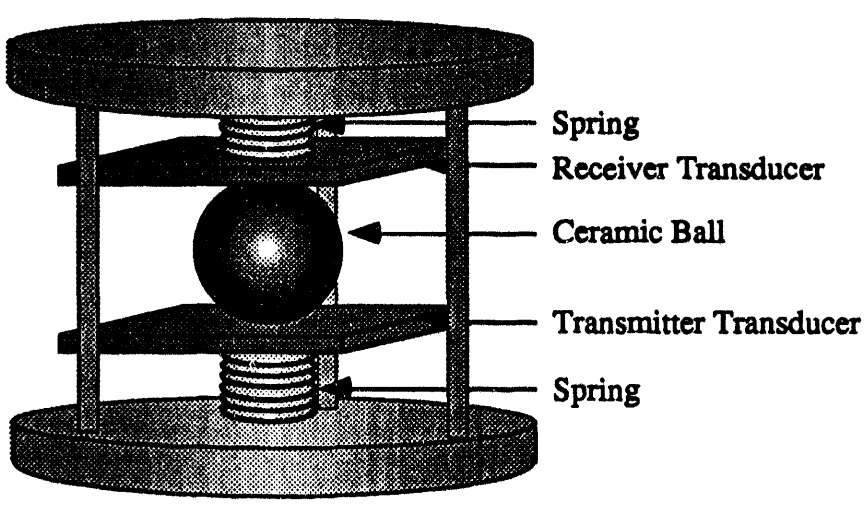

Figure 3.2 Zoom-in look of the transducer-sphere set, the two transducers are mounted on springs.

$$s_1 \sin[2\pi f_1 t + \phi_{s1}]. \tag{3.1}$$

where for simplicity, we assume the outputs from both channels of synthesizer 1 to have the same amplitude s_1, frequency f_1, and phase ϕ_{s1}.

We can write the acoustic signal output from transducer 1 as

$$s_1 t_1 \sin[2\pi f_1 t + \phi_{s1} + \phi_{t1}], \tag{3.2}$$

where t_1 and ϕ_{t1} are the amplitude and phase conversion factor of transducer 1. The resonant acoustic signal at the north pole of the ball is

$$s_1 t_1 b \sin[2\pi f_1 t + \phi_{s1} + \phi_{t1} + \phi_b], \tag{3.3}$$

where b and ϕ_b are the amplitude factor and phase change of the wave propagating through the ball. This acoustic signal at the north pole is converted by transducer 2 to an electric signal

$$s_1 t_1 b t_2 \sin[2\pi f_1 t + \phi_{s1} + \phi_{t1} + \phi_b + \phi_{t2}]. \tag{3.4}$$

where t_2 and ϕ_{t2} are the amplitude and phase conversion factor of transducer 2. This signal is mixed by mixer 1 with output from synthesizer 2,

$$s_2 \sin[2\pi f_2 t + \phi_{s2}]. \tag{3.5}$$

where for simplicity, we assume the outputs from both channels of synthesizer 2 to have the same amplitude s_2, frequency f_2, and phase ϕ_{s2}. The output from mixer 1 contains two signals, namely

$$\frac{-1}{2}s_1s_2t_1t_2b\,cos\left[2\pi(f_1+f_2)t+(\phi_{s1}+\phi_{s2}+\phi_{t1}+\phi_{t2})+\phi_b\right] \tag{3.6}$$

and

$$\frac{1}{2}s_1s_2t_1t_2b\,cos\left[2\pi(f_1-f_2)t+(\phi_{s1}-\phi_{s2}+\phi_{t1}+\phi_{t2})+\phi_b\right], \tag{3.7}$$

plus higher harmonics. This set of two signals is sent into the signal channel of the lock-in amplifier. On the other hand, there are two signals being fed into mixer 2: from synthesizer 1:

$$s_1\,sin\left[2\pi f_1t+\phi_{s1}\right], \tag{3.8}$$

and from synthesizer 2:

$$s_2\,sin\left[2\pi f_2t+\phi_{s2}\right]. \tag{3.9}$$

The output from mixer 2 contains two signals, namely:

$$\frac{-1}{2}s_1s_2\,cos\left[2\pi(f_1+f_2)t+(\phi_{s1}+\phi_{s2})\right] \tag{3.10}$$

and

$$\frac{1}{2}s_1s_2\,cos\left[2\pi(f_1-f_2)t+(\phi_{s1}-\phi_{s2})\right], \tag{3.11}$$

plus higher harmonics. This set of two signals is sent into a low-pass filter set at 5KHz. Since

$$f_2=f_1-5\text{KHz}, \tag{3.12}$$

the output from the low-pass filter contains only the signal (3.11), i.e., $(1/2)s_1 s_2 \cos[2\pi(f_1 - f_2)t + (\phi_{s1} - \phi_{s2})]$, a 5KHz signal. This 5KHz signal is fed into the reference channel of the lock-in amplifier. The lock-in amplifier locks onto the 5KHz component of the signal being sent into the signal channel, i.e., the expression given by (3.7). The lock-in amplifier has two outputs, the amplitude of the locked-in signal sent into the signal channel given by (3.7), and the phase difference between the reference channel signal (3.11) and the lock-in signal (3.7). Therefore, the amplitude output should be

$$\frac{1}{2} s_1 s_2 t_1 t_2 b, \tag{3.13}$$

and the phase reading should be

$$\phi_{t1} + \phi_{t2} + \phi_b \tag{3.14}$$

Combining expressions (3.13) and (3.14) with the definition of the resonance quality factor[5]:

$$Q = \frac{\text{Resonance Frequency}}{\text{3 dB Bandwidth}}, \tag{3.15}$$

it is seen that if the operation is at 10MHz, the 3dB bandwidth will be around 1KHz for a quality factor in the order of 10,000, which is typical for the resonances of ceramic bearing balls. The two transducers in this experiment are excited at frequencies off resonance and their responses within a narrow frequency range, say 10 KHz, are very flat. Therefore, for each resonance peak of the sphere, we can treat t_1, t_2, ϕ_{t1}, and ϕ_{t2} as constants. In addition, s_1 and s_2 are fixed setting values on each synthesizer and are constants. It can be concluded that for each resonance peak, the amplitude (3.13) measured by the lock-in amplifier is proportional to the actual acoustic resonance signal at the north pole of the sphere; also, the phase (3.14) measured by the lock-in amplifier is the actual phase of the acoustic signal offset by a constant which is a characteristic of the pair of transducers.

3.4 Experiment Results and Analysis

3.4.1 Low Frequency Measurement

Three Si_3N_4 ceramic bearing balls of 1/2 inch diameter were used as samples for the experiment. The first ball is perfect with no cracks. The second ball has a series of cracks made with a 10 g load on a Knoop indenter; and the third ball has cracks made with a load of 50 g on the indenter. We will refer to these three balls as balls A, B, and C, respectively. We measured phase and amplitude of the resonant frequency spectrum of the spheres. Local maxima in amplitude are used to determine the resonance frequencies of the sphere, whereas the phase of the spectrum is used to measure the resonance Q's.

There is an important reason why we want to measure both amplitude and phase. Using amplitude alone to measure samples with high Q's is time consuming because of the small frequency increment necessary for an accurate measurement. The importance of phase measurement is evident for the following reason: near resonance, the phase curve is almost a straight line. The phase undergoes a change of π on passing through resonance and its slope at resonance is:[5]

$$\frac{d(\text{phase})}{d(\text{frequency})} = \frac{d\theta}{df} = -\frac{2Q}{f_0} \tag{3.16}$$

which is a constant. The equation for the phase near resonance is given by:

$$\theta = \theta_0 - \tan^{-1}\frac{\left(f^2 - f_0^2\right)Q}{ff_0} \tag{3.17}$$

where θ_0 is the phase value at resonance, f_0 is the resonance frequency, f is the frequency at each point, and Q is the quality factor. This characteristic equation is commonly observed also in resonant electric circuits for large values of Q.

Therefore, to determine the resonance Q for a particular mode, we simply determine the resonant frequency to the desired accuracy by amplitude measurement, measure several points around resonance, and fit a curve to the measured phase according to the above equation.

We determine the mechanical properties of the samples following the procedures shown in the flow chart in Figure 3.3. We note from the discussion following the characteristic equation of torsional resonances, in equation (2.24)

$$(n-1)J_{n+1/2}(\eta) - \eta J_{n+3/2}(\eta) = 0 \tag{2.32}$$

that the resonant frequencies of the torsional resonances are only dependent upon radius of sphere a and shear wave velocity V_s ($\eta = 2\pi fa/V_s$). If we are able to accurately

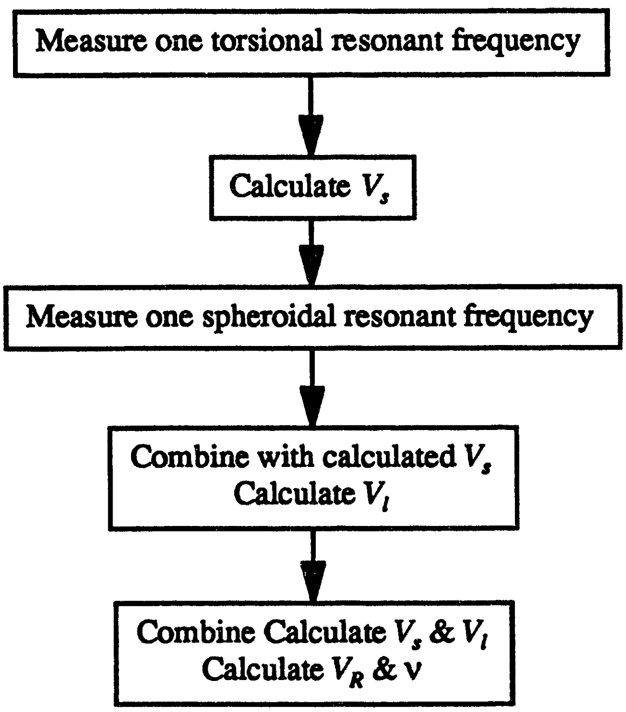

Figure 3.3 Flow chart of material acoustic property measurement using the resonant sphere technique.

measure the resonance frequency of one of the torsional modes, we should be able to use equation (2.24) to calculate V_s accurately. Given the definition

$$Q = \frac{\text{Resonance Frequency}}{\text{3 dB Bandwidth}}, \tag{3.15}$$

it is understood that high Q modes have a smaller 3 dB bandwidth and are therefore more frequency selective. For resonance frequency measurement, it is desirable to choose a particular high Q mode to perform accurate resonance frequency measurement.

Similarly, the third step in Figure 3.3 is to find a high Q spheroidal mode and measure its resonance frequency. Combining the measured spheroidal mode resonance frequency and calculated V_s from step two, the longitudinal wave velocity V_l can be calculated using the characteristic equation of spheroidal mode resonance,

$$\frac{2k_l}{k_s}\left[\frac{1}{\eta}+\frac{(n-1)(n+2)}{\eta^2}\left(\frac{J_{n+3/2}(\eta)}{J_{n+1/2}(\eta)}-\frac{n+1}{\eta}\right)\right]\frac{J_{n+3/2}(\xi)}{J_{n+1/2}(\xi)}$$
$$+\left[-\frac{1}{2}+\frac{(n-1)(n+2)}{\eta^2}+\left(\frac{1}{\eta}-\frac{2n(n-1)(n+2)}{\eta^3}\right)\frac{J_{n+3/2}(\eta)}{J_{n+1/2}(\eta)}\right]=0 \qquad (2.39)$$

where $\xi = 2\pi fa/V_l$, k_l and k_s are the wave numbers of longitudinal and shear waves, respectively.

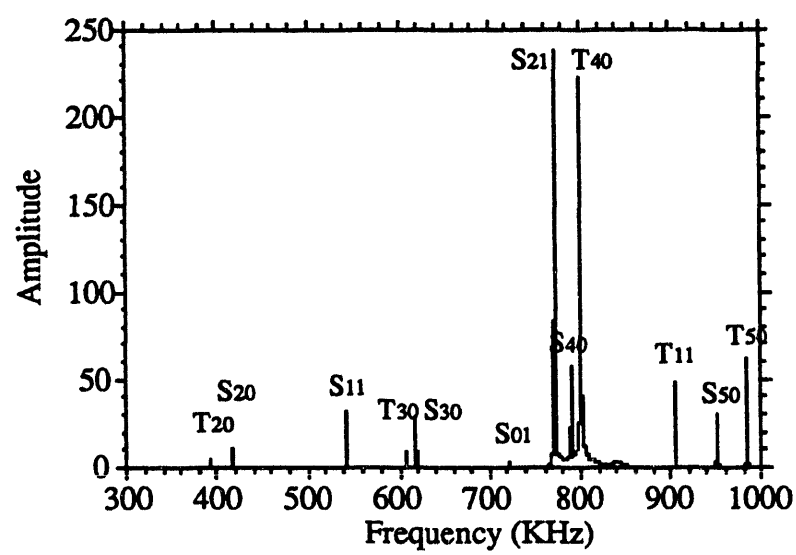

Figure 3.4 Typical low frequency amplitude spectrum for ceramic bearing balls with diameter 1/2 inch.

Figure 3.4 shows an example of the amplitude frequency spectrum of ball C, the 1/2 inch diameter Si_3N_4 ceramic bearing ball which has a series of cracks made by a 50 g Knoop indenter. Compared with the mode chart in Figure 2.8, the contact-contact resonant sphere technique is capable of generating all the low frequency resonances. Each peak in Figure 3.4 can be identified to correspond to a theoretically calculated resonance mode in Figure 2.8.

As discussed previously, our experimental technique enables us to mix the resonance acoustic signal down to a low frequency so that the lock-in amplifier can measure the phase of the signal. In figure 3.5 we zoom in on the frequency spectrum in both the amplitude and phase of a particular high Q mode T_{12} of ball A, the ball with no defect. Among the numerous torsional modes of a sphere, the T_{n2} modes had the

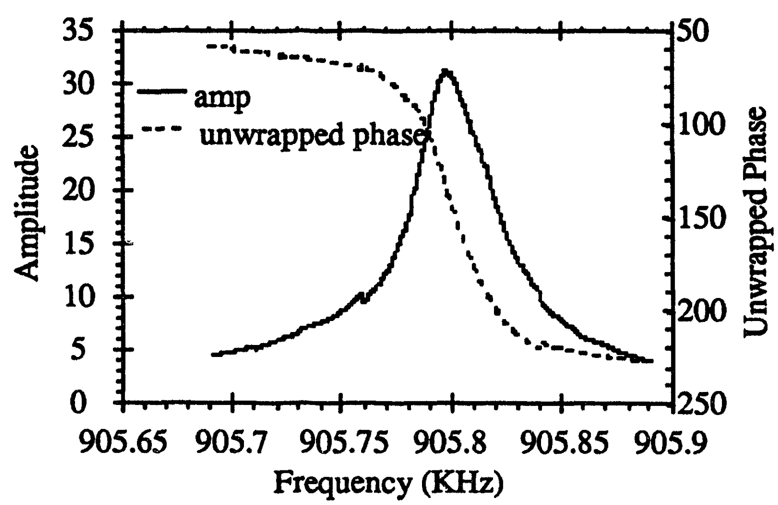

Figure 3.5 T_{12} mode, a high Q mode used for calculating shear wave velocity V_s. We can see clearly the phase transition of 180° near resonance.

	Ball A	Ball B	Ball C
f_{T12} (KHz)	905.80	905.74	905.50
Q_{T12}	34799	42242	32985
f_{S01} (KHz)	720.41	724.42	721.40
Q_{S01}	20058	19245	16918
V_S (m/s)	6270.5	6270.1	6268.4
ν	0.26447	0.26573	0.26522
V_l (m/s)	11081	11100	11082
V_R (m/s)	5779.9	5780.8	5778.8

Table 3.1 Data on spherical resonances obtained by the resonant sphere technique for three ceramic bearing balls, each with a diameter of 1/2 inch. Ball A is a perfect ball with no cracks. Ball B had a series of cracks made with a 10 g load on a Knoop indenter, and Ball C had the cracks with a load of 50 g on the Knoop indenter.

highest Q. The reason is that the large displacement amplitudes of the $\mathbf{T}_{n2}$ modes are mainly inside the sphere. Therefore the contact load between the two transducers and the sphere has little effect on the Q of the resonance. High Q modes are more frequency selective, and are chosen to calculate the mechanical properties. A rough estimation of the accuracy of the measurement is as follows: Given

$$Q = \frac{f}{\Delta f}, \tag{3.22}$$

for a particular torsional mode such as

$$2\pi f a = \text{constant} \cdot V_s, \tag{3.23}$$

where the constant is the theoretical value of the normalized frequency in the mode chart. Therefore,

$$2\pi a \Delta f = \text{constant} \cdot \Delta V_s. \tag{3.24}$$

Divide (3.24) by (3.23) and utilize (3.22), we get

$$\frac{\Delta V_s}{V_s} = \frac{\Delta f}{f} = \frac{1}{Q}. \tag{3.25}$$

Equation (3.25) tells us that the accuracy of acoustic wave velocity measurement is of the same order of magnitude as the reciprocal of the quality factor of the resonance mode. As shown in table 3.1, where we list the material constants calculated from the resonant frequencies for the three samples, the two resonance modes selected, T_{12} and S_{01} modes, are two particular high Q modes. The values for surface wave velocity V_R in the table are calculated according to the curve fitting equation in equation (2.23). From Table 3.1, we deduce several important conclusions about low frequency measurements of spherical resonances. First, the resonance modes selected here have quality factors of the order of 10^4. Equation (3.25) thus predicts an accuracy of material property measurement to be in the order of one part in 10^4. This is confirmed by considering the variation of material property values shown in the table. Second, we conclude from the data that low frequency measurement results are not sensitive to the existence of surface defects and do not reflect the existence of surface defects since low frequency resonances are mainly bulk wave resonances.

3.4.2 High Frequency Measurement

In the higher frequency region, the resonance spectrum becomes more complicated as there is an increasing number of closely spaced higher-order resonance modes. Still, it is possible to isolate the surface wave resonances when the frequency is high enough. In section 2.2.3 we showed the existence of surface acoustic waves in the high frequency region. As shown in Table 3.1, the surface wave velocity of the Si_3N_4 ceramic material used to make our sample is $V_R \approx 5780 m/s$. For

$$\frac{2\pi f a}{V_R} = \frac{2\pi a}{\lambda_R} = k_R a = n = 100, \tag{3.26}$$

this corresponds to an operating frequency of around 14.3 MHz. We operated the contact-contact resonance setup at this frequency region. A typical measurement result is shown in Figure 3.6. Plot (a) of Figure 3.6 is the spectrum of Ball A. Plots (b), (c), and (d) will be discussed later in this section. From plot (a), we observe several dominant resonance modes that are almost equally spaced in the frequency domain. Several reasons lead us to conclude that these dominant modes are indeed surface wave resonance modes. First, because most of their energy is stored near the surface, surface waves are easily excited and detected, therefore, they tend to dominate in the higher frequency region. Second, at the end of chapter 2, we discussed the condition for surface wave resonance on a sphere. We found that to form a surface wave resonance, the circumference of the sphere has to be an integral number of surface wavelength. We combine the calculated data for V_R from Table 3.1 with our measured high frequency resonance frequencies, and calculate the corresponding surface wave length at these resonance frequencies to be:

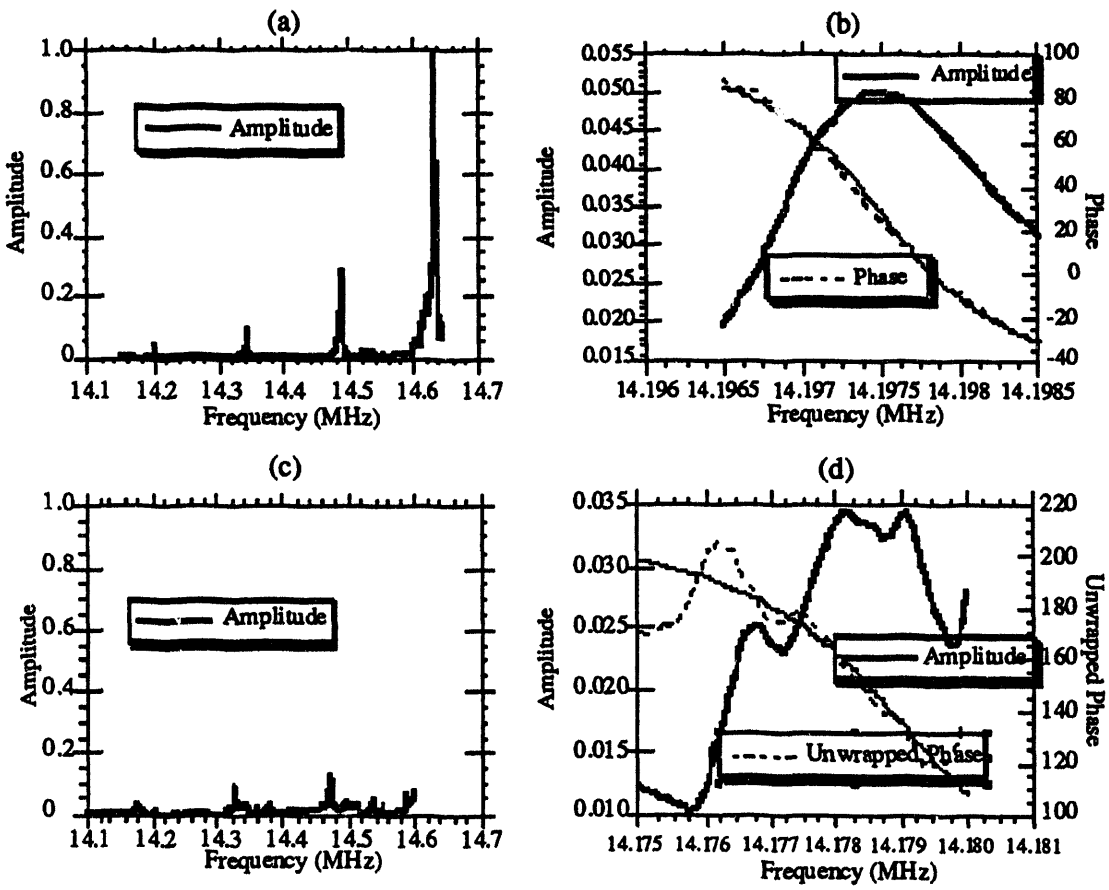

Figure 3.6 Surface wave resonance amplitude spectra for Ball A and Ball C. The dominance of surface wave is evident.

$$\lambda_R = \frac{V_R(\text{calculated})}{f(\text{measured})}. \tag{3.27}$$

We then ascertain that there is an integer number of surface wavelength that fit on one circumference of the sphere. According to the relationship given by equation (3.26), this large integer n is around 100 in this case. This also explains our observation of these equally spaced resonance peaks. For large values of n, the resonance frequency f_n is easily derived from equation (3.26) as:

$$f_n = \frac{nV_R}{2\pi a}. \tag{3.28}$$

Therefore, the peak-peak distance in the frequency domain is given by:

$$\Delta f = f_n - f_{n-1} = \frac{nV_R}{2\pi a} - \frac{(n-1)V_R}{2\pi a} = \frac{V_R}{2\pi a} = \text{constant} \tag{3.29}$$

The experimentally measured values of the resonance Q's for the dominating modes are of similar value, which indicates that these modes are of similar character. We therefore conclude that these dominant modes are surface wave modes. It has to be noted here that it is almost impossible to use the mode chart in Figure 2.8 to identify the surface wave resonance modes because there are so many different higher order harmonics in the high frequency region.

In figure 3.6, we show four spectra plots, two for Ball A, two for Ball C. Plots (a) and (b) are the spectra of Ball A, where (b) is a zoom-in plot which also shows the phase information, the thin solid line in (b) is the curve fitting of the phase using equation (3.17). Plots (c) and (d) are the spectra of Ball C, where (d) is a zoom-in plot which also shows the phase information, the thin solid line in (d) is the curve fitting of the phase

	Ball A		Ball B		Ball C	
$2\pi a / \lambda_R$	f (MHz)	Q	f (MHz)	Q	f (MHz)	Q
98	14.1975	10810	14.2090	7905	14.1790	3655
99	14.3406	11321	14.3547	7998	14.3252	4348
100	14.4846	9573	14.4988	8546	14.4677	4607

TABLE 3.2 Data obtained by the resonant sphere technique for three ceramic bearing balls, each with a diameter of 1/2 inch. Ball A is a perfect ball with no cracks. Ball B had a series of cracks made with a 10 g load on a Knoop indenter, and Ball C had the cracks with a load of 50 g on the Knoop indenter. V_R is the surface wave velocity, and $\lambda_R = V_R/f$ is the wavelength of the surface wave at frequency f.

using equation (3.17). When we compare (a) with (c), we see qualitatively that the spectrum of Ball C is much noisier than that of Ball A. When zooming in on one of the resonance peaks, as shown in (b) and (d), we see that the spectrum for Ball C is split while the spectrum for Ball A is quite smooth near resonance. Both of these two phenomena are probably due to the interaction between the original surface wave and the surface waves scattered by the surface defects. The spectra of ball B are similar to those of ball C, but the effect of the cracks on the quality of resonances is less severe.

Table 3.2 summarizes the measurement results of the three balls A, B and C for three surface wave resonance modes. We note that the Q of the surface wave resonances decreases by as much as 50~60% as the load on the indenter, and consequently, the size of the surface cracks increases. Thus we have a direct relationship between the value of the Q of the surface wave resonance and the density of surface defects.

The physical definition of quality factor Q is

$$Q = \frac{2\pi \cdot \text{Maximum Stored Energy}}{\text{Power Dissipation per Cycle}}. \tag{3.30}$$

The numerator is the maximum stored energy in the acoustic resonance of the sphere. The power dissipation term in the denominator consists of several parts: power loss due to viscous damping in the material, power loss due to leakage of surface wave energy into the air, and power loss due to scattering from surface defects. Surface defects scatter surface wave energy into two parts: the first part is scattered surface waves and the second part is scattered bulk waves. The scattered surface wave interferes with the original incident surface wave, and the energy lost into bulk does not contribute to surface wave energy at all. Therefore, the larger the crack size, the more significant the loss mechanism and the larger the denominator of equation (3.30). We conclude that as crack size increases, the value of Q decreases.

3.5 Concluding Remarks for the Contact-Contact Resonance Sphere Technique

In this chapter, we described our development of the contact-contact resonance sphere technique. We developed a computer controlled system that is capable of measuring the frequency spectrum of a sphere in both amplitude and phase. We showed also the high degree of accuracy of our measurements in determining the material properties (one in 10^4 accuracy). From experiment conducted in the high frequency region, we demonstrated experimentally, for the first time, the existence of surface waves on spheres. We showed in Table 3.1 that low frequency measurement is good for material property measurement, and has no direct relationship with surface defect. In the high frequency region, as shown in Table 3.2, we observed a one to one correspondence between crack size and surface wave resonance Q. It has to be noted here that it is extremely important to control the alignment between the two transducers and the pressure load between the transducer and the sphere. The effect of the loading is especially significant when operated in the high frequency region, when the experiment procedure about loading and unloading the transducers described in section 3.2 is properly followed, the results are repeatable. This loading problem motivated us to develop the non-contacting detection scheme which is discussed in chapter 4.

REFERENCES

[1] D. B. Fraser and R. C. LeCraw, *Novel Method of Measuring Elastic and Anelastic Properties of Solids*, Rev. Sci. Inst. **35**, 1113-1115 (1964).

[2] Naohiro Soga and Orson L. Anderson, *Elastic Properties of Tektites Measured by Resonant Sphere Technique*, J. Geoph. Res. **72**, 1733-1739 (1967)

[3] M. R. Notis, R. M. Spriggs, and W. C. Hahn, Jr., *Elastic Moduli of Pressure-Sintered Nickel Oxide*, J. Geoph. Res. **76**, 7052-7061 (1971).

[4] C. P. Hsieh and B. T. Khuri-Yakub, *Surface Defect Inspection of Spherical Objects by the Resonant Sphere Technique*, Appl. Phys. Lett. **60** (15) (1992).

[5] James W. Nilsson, in *Electric Circuits*, Addison-Wesley, MA (1986)

Chapter 4

Laser-Ultrasound: One-Point-Contact Measurement

4.1 Introduction

In the previous chapter, we described the method of the contact-contact resonance sphere technique. This technique is operable in two frequency regions. In the low frequency region, the technique can accurately characterize (one in 10^4) acoustic material properties such as longitudinal wave velocity, shear wave velocity, and Poisson's ratio. In the high frequency region, where surface wave resonance dominates, it can be used to perform surface defect inspection. The existence of surface defects significantly reduces the quality factor of surface wave resonance modes. However, this technique has certain limitations, particularly in the measurement of small spheres. The first limitation is in the proper alignment of the two transducers, because the transducers are mounted on springs to simulate the free oscillation condition of the sphere. The second limitation is in controlling the contacting load between the transducers and the sphere. As the sphere gets smaller, the contact pressure and area between the transducers and the sphere can no longer be ignored. These problems can be circumvented by a one-point-contact measurement technique, in which the sample is supported by a concave depression in a buffer rod bonded to a transducer. This technique uses only one point to support the sphere as well as excite resonances on the sphere. The resonance signal is detected using an optical interferometer which measures the displacement of the top surface of the sphere, a non-contacting detection scheme.

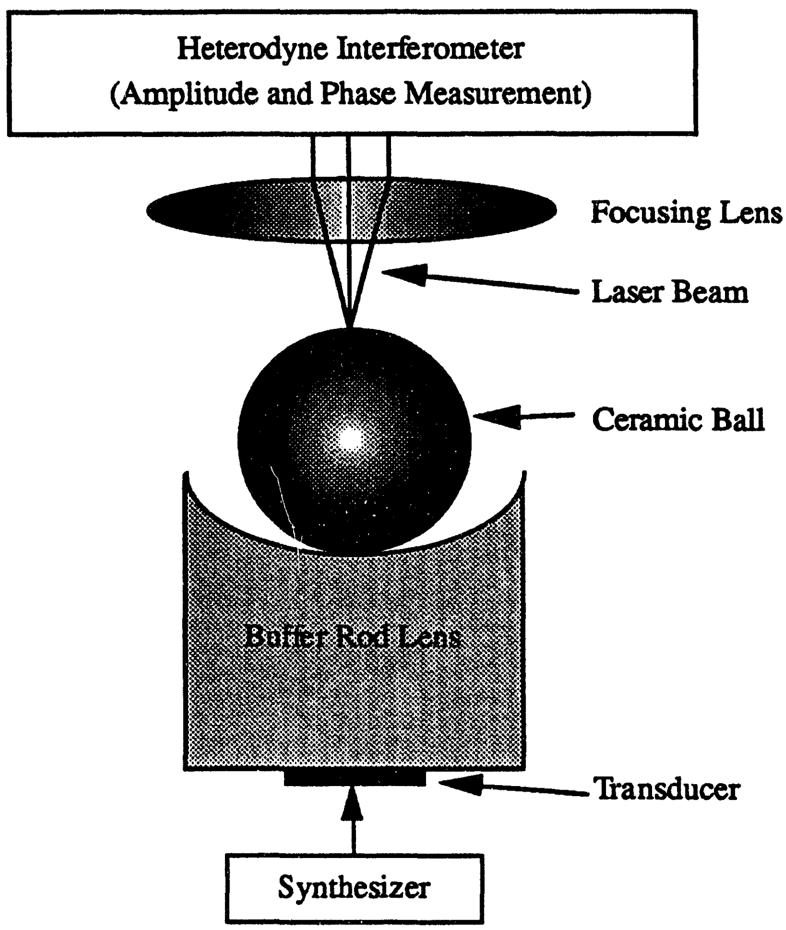

Figure 4.1 One-Point-Contact measurement experimental setup.

4.2 Experimental Setup

Figure 4.1 shows the schematic of the one-point-contact technique. The ball is placed on a spherical depression (lens) in a buffer rod with a longitudinal piezoelectric transducer on the other end. The radius of curvature of the lens is larger than that of the ball, so that the ball can rest at the bottom of the lens. The transducer excites resonances on the ball and the interferometer measures vertical displacements of the waves on the ball at the opposite pole.

4.2.1 Hertzian Contact

The only contact between the sphere and the external environment is a single Hertzian contact with a diameter of d given by[1]:

$$d = 2F^{\frac{1}{3}}\left(\frac{DRR'}{R-R'}\right)^{\frac{1}{3}} \tag{4.1}$$

where
$$D = \frac{3}{4}\left(\frac{1-\nu^2}{E}+\frac{1-\nu'^2}{E'}\right) \tag{4.2}$$

and R, ν, E are the radius, Poisson's ratio, and Young's modulus of the lens, R', ν', E' are the radius, Poisson's ratio, and Young's modulus of the sphere, and F is the total contact force (i.e., weight of the sphere).

For a fused quartz buffer rod, $\nu \approx 0.1694$ and $E \approx 7.274*10^{10}\,Newton/m^2$. For a hot isostatically pressed Si_3N_4 ceramic (NBD 200), $\nu' \approx 0.2616$, $E' \approx 3.223*10^{11}\,Newton/m^2$, and density $\approx$ 3270 Kg/m^3. In Figure 4.2 we show two calculation results. The first one shows curves for contact diameter versus radius of a Si_3N_4 ceramic ball sitting on a fused quartz buffer rod. Each curve stands for a different radius of curvature of the depression on the buffer rod. In figure 4.2, we also show an extreme case where there is no depression (R = infinity). The second plot shows the contact diameter versus the radius of curvature of the concave depression on the buffer rod. We see that for each size of ball, the contact diameter varies only slowly with the radius of curvature of the depression when it is sufficiently larger than the radius of the ball.

For example, with $R = 4$ mm, a 1 mm diameter ceramic ball with $R' = 0.5\ mm$, we calculate $d \approx 0.45\ \mu m$. At 60 MHz, where the surface wavelength on ceramics is around 100 μm, the contact diameter is only about one percent of the wavelength, and thus has little effect on the propagation of surface waves.

To calculate the relationship between radius of ball and radius of curvature of the depression for most efficient surface wave excitation, the contact diameter should be equal to $\lambda_R/2 = V_R/(2f)$, where f (Hz) is the operating frequency, and λ_R and V_R are the surface wavelength and surface wave velocity on the ball, respectively. For Si_3N_4 ceramics, $V_R \approx 5758.5$ m/sec, the relationship between radius of ball R' and radius of curvature of the depression R for most efficient surface wave excitation is

$$R = \frac{R'}{1 - 5.5928 \cdot 10^{-17} \times f^3 \times R'^4} \tag{4.3}$$

Figure 4.3 shows the optimum radius of curvature of the depression versus operating frequency for 5 particular radii of ceramic balls.

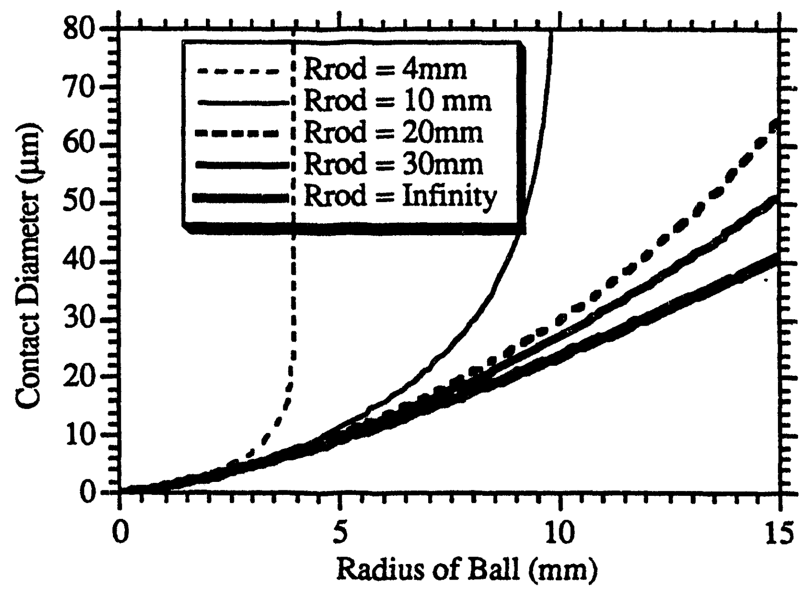

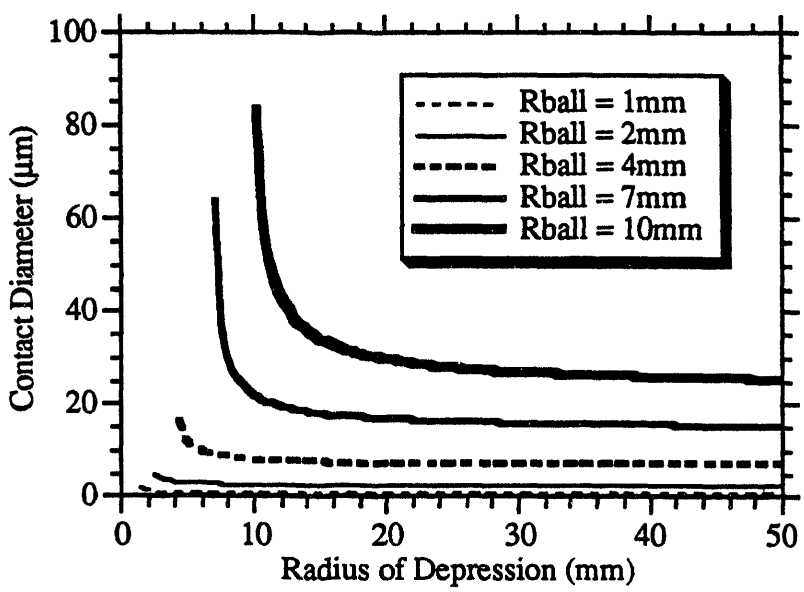

Figure 4.2 (a) Hertzian contact diameter versus radius of ceramic ball.

(b) Hertzian contact diameter versus radius of rod depression

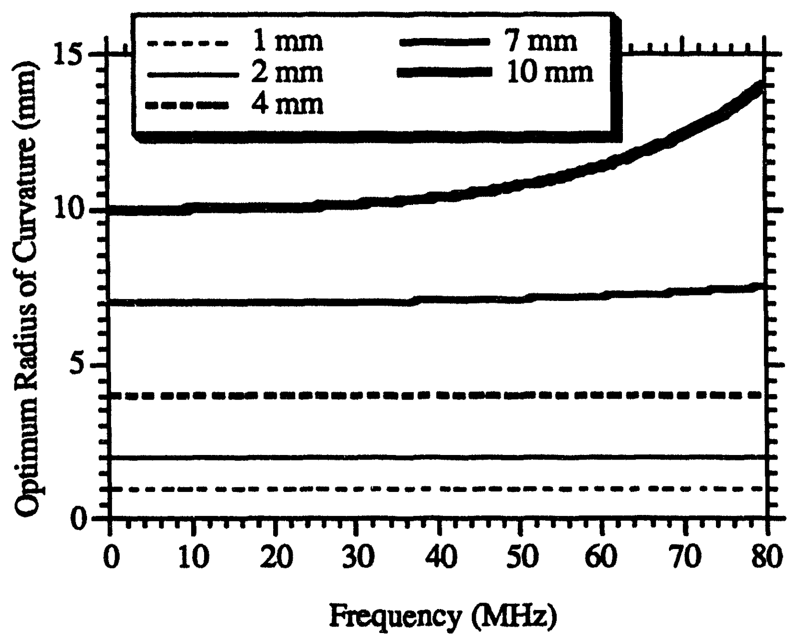

Figure 4.3 Optimum radius of curvature of the depression versus operating frequency for 5 different radii of ceramic balls

It is to be noted here that we are interested in measuring resonance spectra. Therefore, in order to keep the resonance Q high the coupling to the ball should be weak, so the contact diameter should be much smaller than 1/10 of the surface wavelength in order not to interfere with the propagation of surface waves. For fused quartz buffer rod and Si_3N_4 ceramic ball, the minimum radius of curvature of the depression becomes:

$$R > \frac{R'}{1-6.991\cdot 10^{-15} f^3 R'^4} \qquad (4.3.a)$$

Figure 4.4 shows the minimum radius of curvature required for the depression on a fused quartz buffer rod with different radii of Si_3N_4 balls.

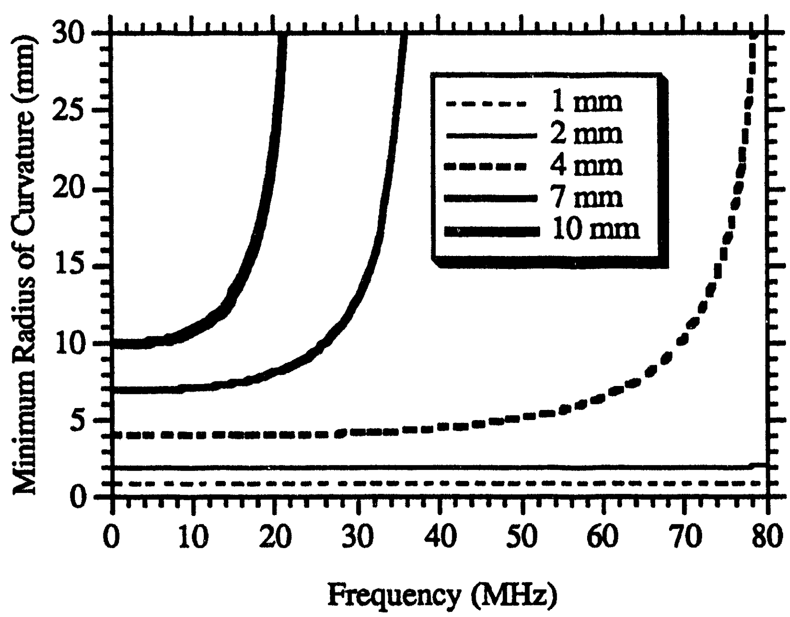

Figure 4.4 Minimum radius of curvature of the spherical depression for a Hertzian contact less than 1/10 of surface wavelength.

We can also combine results of equation (4.3.a) with the condition for generating true surface waves that requires $k_R a > 100$. For example, for a Si_3N_4 ball with radius 4mm, to generate true surface waves, the frequency has to be higher than 23MHz, this corresponds to a minimum radius of curvature require for the depression of only 4.089mm.

4.2.2 Advantages Of The One-Point-Contact Technique

The one-point-contact technique has advantages over the contact-contact technique because it does not require alignment of the two transducers. Also, the contacting load between the ball and the transducer is predictable. An experiment similar to the one-point-contact technique has been performed by Royer and Shui where a sphere was placed on a three-point mount and resonance was excited photoacoustically by a modulated laser beam[2]. The ball had a diameter of 20 mm and was made of stainless steel with 13% of chromium. They determined the shear wave velocity and the longitudinal wave velocity with a delay line method with an accuracy with 0.1% and measured $V_s = 3290$ m/sec and $V_l = 5988$ m/sec. They calculated V_R to be 3061 m/sec. They reported the observation of low frequency surface wave resonance modes up to $k_R\, a \approx 40$ which corresponds to a maximum operating frequency of 1.95 MHz.

Our technique has several advantages over this earlier technique. First, the only contact between the sphere and the external environment is a Hertzian contact. The effect of this contacting point on the resonance of the sphere is negligible as discussed in the last section. Second, it is more efficient to excite resonance by a direct mechanical contact. The surface displacement of the transducer piezoelectric material $LiNbO_3$, (crystal-type trigonal 3m, propagation along Z axis), active area 1 mm^2, center frequency 150 MHz, fused quartz rod length 30 mm, with an input of 1 volt, is shown in figure 4.5. The top plot shows a frequency response between DC and 5MHz, the bottom plot shows a frequency response up to 300MHz. The resonant spectrum in the low frequency is due to resonance of the buffer rod, it disappears in the high frequency region because of attenuation inside the buffer rod. We see that we can acoustically excite a strong displacement on the ball. Since the photoacoustic effect on ceramics is very weak,[3] to generate surface waves using laser excitation will have the risk of damaging the sample. The laser for the interferometer in our setup is a He-Ne laser with a power of 4mW and should have negligible thermal effect on the sphere. Therefore, the measurement can be done at a higher signal-to-noise ratio, compared to the photoacoustic method which is very inefficient on ceramics. Furthermore, because the sphere is always located at the bottom of the concave depression, alignment of the measurement system for different spheres of identical diameters becomes trivial. Finally, there is no limit to the frequency range over which the measurement can be made. We have measured up to a $k_R a$ value of 240, in this case, a 1/4 inch diameter ceramic bearing ball with an excitation up to 70 MHz.

4.2.3 Optical Detection And Heterodyne Interferometer

An excellent paper written by Jean-Pierre Monchalin reviews various optical methods to detect ultrasound at the surface of opaque solids[4]. Optical detection techniques for ultrasound can be classified into non-interferometric techniques and interferometric techniques. The former are well developed and of limited application, while the latter are more general and are presently the object of active developments.

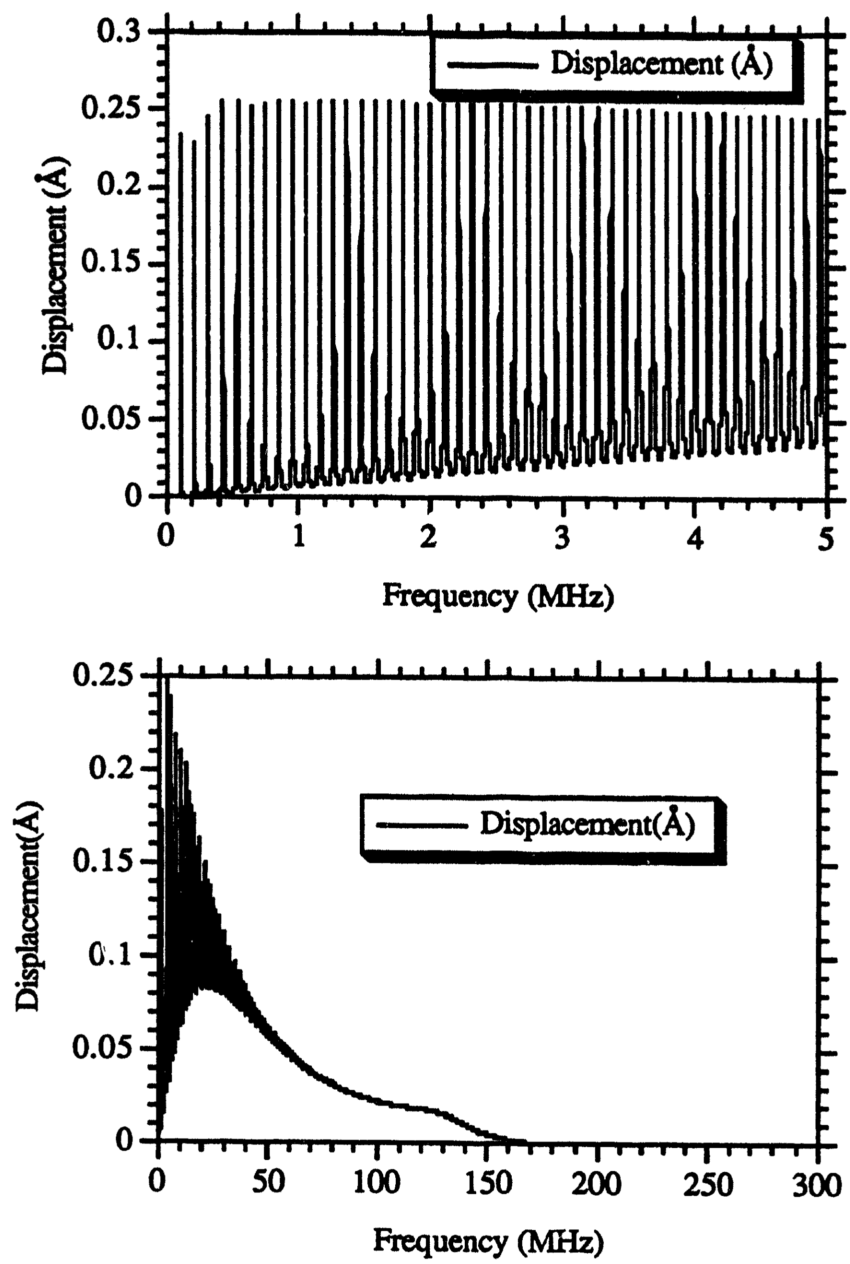

Figure 4.5 Displacement of the transducer used. ($LiNbO_3$ crystal-type trigonal 3m, propagation along Z-axis, active area $1mm^2$, center frequency 150 MHz, fused quartz rod length 30mm, with an input of 1 volt)

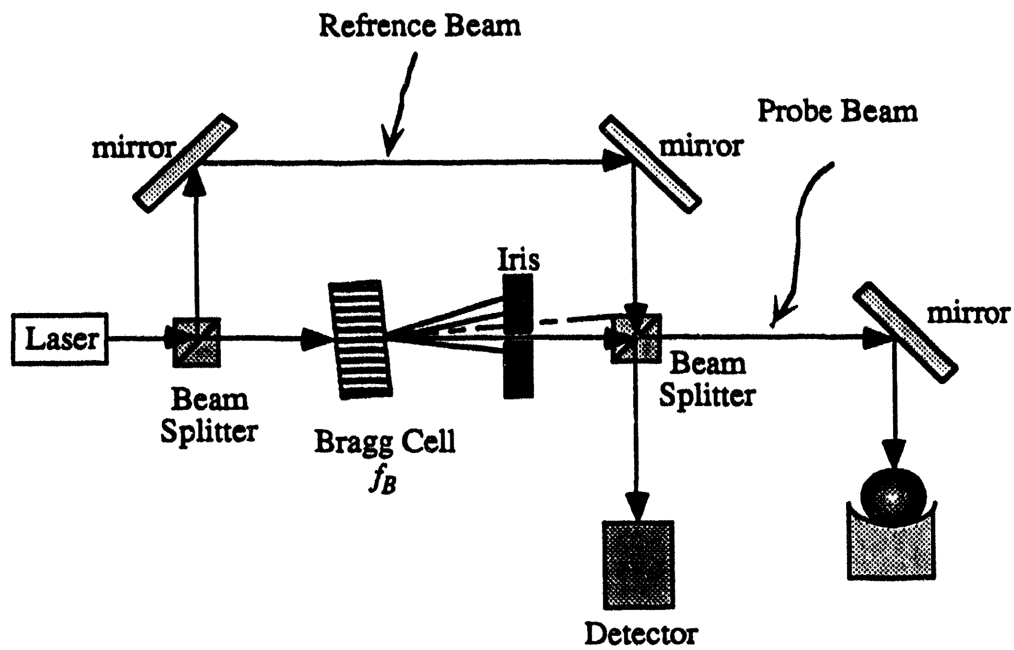

Figure 4.6 Optical Heterodyne Interferometer configuration for spherical resonance detection.

There are several optical techniques used to detect ultrasound that are not based on interferometry: the knife-edge technique[5,6,7,8,9,10,11], the surface-grating technique[12,13], the reflectivity technique[14,15], and a technique based on a light filter[16,17]. All these techniques give a filtering bandwidth that is fixed and determined by the medium, unlike interferometry, which enables one to choose the most suitable bandwidth easily.

There are various interferometric detection techniques that can be classified into the following three types: optical heterodyning interferometry[18,19,20,21,22], differential interferometry[23,24], and velocity or time-delay interferometry[25,26]. Of these different interferometric detection techniques, optical heterodyning interferometry is the most commonly used, and is employed in our experiment. The configuration of our heterodyne interferometer is shown in figure 4.6[27].

The output of a low noise He-Ne laser is split into two parts. One part, the beam in the reference arm, is reflected twice by the two mirrors and sent directly into the photo detector. The second part is sent into a Bragg cell, an acousto-optic modulator, in our case driven at 80 MHz. The output from the Bragg cell consists of several diffraction beams[28]. An iris is used to pass only the first diffraction lobe which is frequency shifted by the Bragg cell frequency. The Bragg cell is rotated to an angle such that the first diffracted beam has maximum intensity, as shown in figure 4.6. We call this first diffraction beam the probe beam. The probe beam is deflected by the mirror and reflected by the north pole of the resonating sphere. The optical phase of the reflected probe beam is modulated by the displacement $u\cos(\omega_a t+\phi_a)$ of the resonating surface, where u, ω_a, and ϕ_a stand for maximum displacement amplitude, angular frequency, and phase of the acoustic displacement at the north pole of the sphere. Theoretically, it is possible to calibrate an optical heterodyne interferometer and measure both the amplitude and the phase of the displacement as will be shown in the following discussion.

We represent the reference beam sent into the photo detector by

$$\hat{R} = R\exp\{j[(\omega_L t+\phi_R+\phi_{RN})]\} \tag{4.4}$$

where R, ϕ_R, and ϕ_{RN} are the amplitude, phase, and phase noise of the reference beam, respectively and ω_L is angular frequency of the laser. The reflected probe signal has the form:

$$\hat{S} = S\,exp\{j[(\omega_L + \omega_B)t + \phi_S + \phi_{SN} + 2K_L u\,cos(\omega_a t + \phi_a)]\}, \tag{4.5}$$

where ω_B is the angular frequency of the Bragg cell; S, ϕ_S, and ϕ_{SN} are the amplitude, phase, and phase noise of the probe beam, respectively; and $K_L = 2\pi/\lambda_L$ is the wave number of the laser beam. For the He-Ne laser, $\lambda_L = 6325$ Å, and $K_L = 1/1007(1/\text{Å})$.

The photo detector detects the intensity of the incident light. Therefore, the output signal from the photo detector is:

$$\begin{aligned}
&|\hat{R} + \hat{S}|^2 = (\hat{R} + \hat{S})(\hat{R}^* + \hat{S}^*) = \\
&[R\,exp\{j[(\omega_L t + \phi_R + \phi_{RN})]\} \\
&+S\,exp\{j[(\omega_L + \omega_B)t + \phi_S + \phi_{SN} + 2K_L u\,cos(\omega_a t + \phi_a)]\}] \\
&\cdot[R\,exp\{-j[(\omega_L t + \phi_R + \phi_{RN})]\} \\
&+S\,exp\{-j[(\omega_L + \omega_B)t + \phi_S + \phi_{SN} + 2K_L u\,cos(\omega_a t + \phi_a)]\}]
\end{aligned} \tag{4.6}$$

where the asterisk stands for complex conjugate. Equation (4.6) can be simplified to be:

$$\begin{aligned}
&|\hat{S} + \hat{R}|^2 = \\
&S^2 + R^2 + 2SR\,cos[\omega_B t + \phi_S - \phi_R + \phi_{SN} - \phi_{RN} + 2K_L u\,cos(\omega_a t + \phi_a)]
\end{aligned} \tag{4.7}$$

For $K_L u \ll 1$ ($u \ll 1007$ Å for He-Ne laser),

$$cos[2K_L u\,cos(\omega_a t + \phi_a)] \approx 1, \tag{4.8}$$

and

$$sin[2K_L u cos(\omega_a t + \phi_a)] \approx 2K_L u cos(\omega_a t + \phi_a) \tag{4.9}$$

Therefore, (4.7) can be expressed as follows:

$$\begin{aligned}
&(S^2 + R^2) + 2SR\{cos(\omega_B t + \phi_S - \phi_R + \phi_{SN} - \phi_{RN}) cos[2K_L u cos(\omega_a t + \phi_a)] \\
&\qquad - sin(\omega_B t + \phi_S - \phi_R + \phi_{SN} - \phi_{RN}) sin[2K_L u cos(\omega_a t + \phi_a)]\} \\
&\approx (S^2 + R^2) + 2SR\{cos(\omega_B t + \phi_S - \phi_R + \phi_{SN} - \phi_{RN}) \cdot 1 \\
&\qquad - sin(\omega_B t + \phi_S - \phi_R + \phi_{SN} - \phi_{RN}) \cdot 2K_L u cos(\omega_a t + \phi_a)\} \\
&= (S^2 + R^2) + 2SR\{cos(\omega_B t + \phi_S - \phi_R + \phi_{SN} - \phi_{RN}) \\
&\qquad - K_L u[sin(\omega_B t + \phi_S - \phi_R + \phi_{SN} - \phi_{RN} + \omega_a t + \phi_a) \\
&\qquad\quad - sin(\omega_B t + \phi_S - \phi_R + \phi_{SN} - \phi_{RN} - \omega_a t - \phi_a)]\} \\
&= (S^2 + R^2) + 2SR cos(\omega_B t + \phi_S - \phi_R + \phi_{SN} - \phi_{RN}) \\
&\quad - 2SRK_L u sin[(\omega_B + \omega_a)t + \phi_S - \phi_R + \phi_{SN} - \phi_{RN} + \phi_a] \\
&\quad - 2SRK_L u sin[(\omega_B - \omega_a)t + \phi_S - \phi_R + \phi_{SN} - \phi_{RN} - \phi_a]
\end{aligned} \tag{4.10}$$

In expression (4.10), we see that the signal output from the photo detector consists of four parts: a DC signal, a signal with angular frequency ω_B, and two signals of equal amplitude but different angular frequencies, one at $(\omega_B + \omega_a)$, another at $(\omega_B - \omega_a)$.

Figure 4.7 shows a typical picture of the output of a spectrum analyzer that monitors the output signal from the heterodyne interferometer as given by expression (4.10). In this case, the DC signal is blocked to protect the spectrum analyzer. As shown in the picture, the main band is the signal at 80 MHz, our Bragg cell operation frequency. The two side bands are of equal amplitude and with equal frequency distance away from

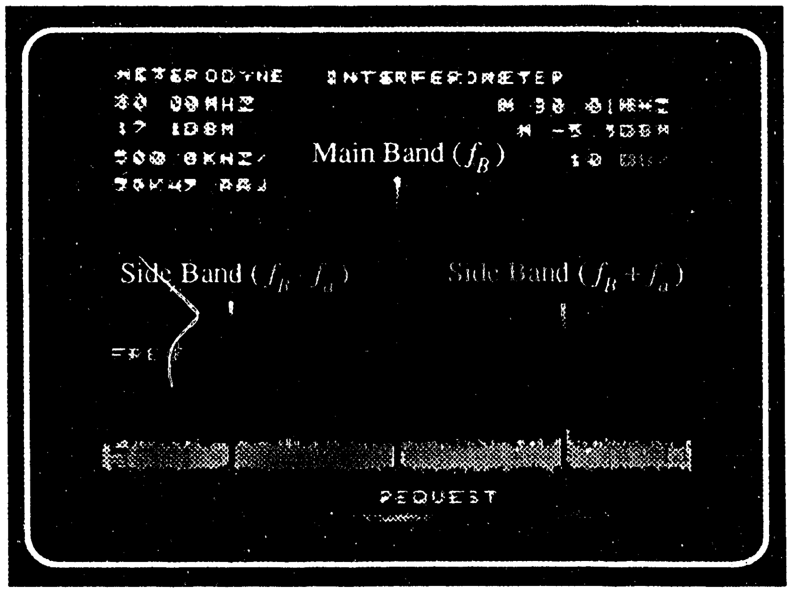

Figure 4.7 A typical picture of the screen of a spectrum analyzer that monitors the output signal from a heterodyne interferometer.

the main band. The frequency difference between the main band and the side band is the frequency of the acoustic signal on the sphere. From the last expression of (4.10), it is observed that the amplitude ratio between the main band and the side band is equal to $1/(K_L u)$. This means the heterodyne interferometer can be calibrated absolutely, and that

$$u = \frac{\text{Amplitude}_{\text{side band}}}{\text{Amplitude}_{\text{main band}}} \frac{1}{K_L} = \frac{\text{Amplitude}_{\text{side band}}}{\text{Amplitude}_{\text{main band}}} \frac{\Lambda_L}{2\pi}, \qquad (4.11)$$

where Λ_L is the wavelength of the laser. For He-Ne laser used in our experiment, $\Lambda_L = 632.8$ *nm*. For this wavelength, equation (4.11) becomes:

$$u = 1007 \frac{\text{Amplitude}_{\text{side band}}}{\text{Amplitude}_{\text{main band}}} \ (\text{Å}) \tag{4.12}$$

To perform broadband detection and acquire the amplitude and phase of the resonance signal, it is necessary to analog signal process the output signal from the interferometer. A schematic of the analog signal processing of the output from the heterodyne interferometer is shown in figure 4.8. The signal from the photo detector (ω_B, $\omega_B \pm \omega_a$) is DC bypassed and then split into two parts. The first part is sent into a phase locked loop. The output from the phased locked loop is an 80 MHz signal whose phase follows the variation of the main band. The second part is low pass filtered, so only (ω_B - ω_a) is passed. These two signals are mixed. The result of the mixing operation is:

$$\begin{aligned}
&2SR\,cos(\omega_B t + \phi_S - \phi_R + \phi_{SN} - \phi_{RN}) \\
&\cdot 2SRK_L u\,sin[(\omega_B - \omega_a)t + \phi_S - \phi_R + \phi_{SN} - \phi_{RN} - \phi_a] \\
&= 2S^2R^2K_L u\,sin[(2\omega_B - \omega_a)t + 2(\phi_S - \phi_R + \phi_{SN} - \phi_{RN}) - \phi_a] \\
&\quad - 2S^2R^2K_L u\,sin[\omega_a t + \phi_a]
\end{aligned} \tag{4.13}$$

The output from the mixer is seen to consist of two parts, one with an angular frequency of $(2\omega_B - \omega_a)$, another with an angular frequency of ω_a. This two part signal is low pass filtered so that only signal at the acoustic frequency is measured. It is observed that this signal is a scaled version of the acoustic signal, and is immune from the phase noise terms. The advantage of using the heterodyne interferometer becomes apparent at this point, where it is apparent that this type of detection scheme is immune from environmental noise (fluctuations in phase). This acoustic signal is further

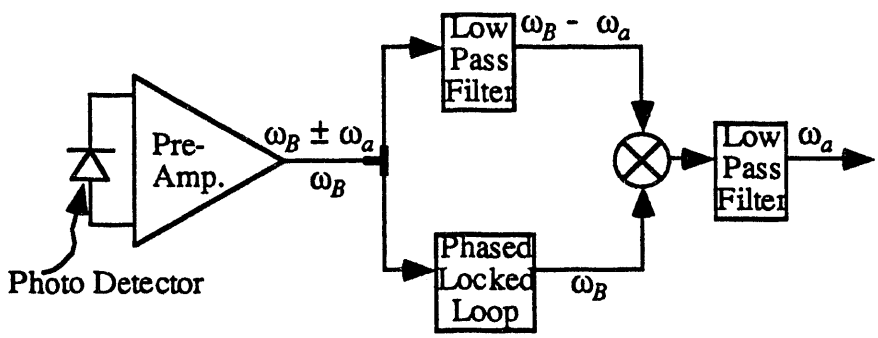

Figure 4.8 Signal analysis of the output of the Heterodyne interferometer

processed using the method discussed in the contact-contact resonance sphere technique in chapter 3 to determine both its amplitude and phase.

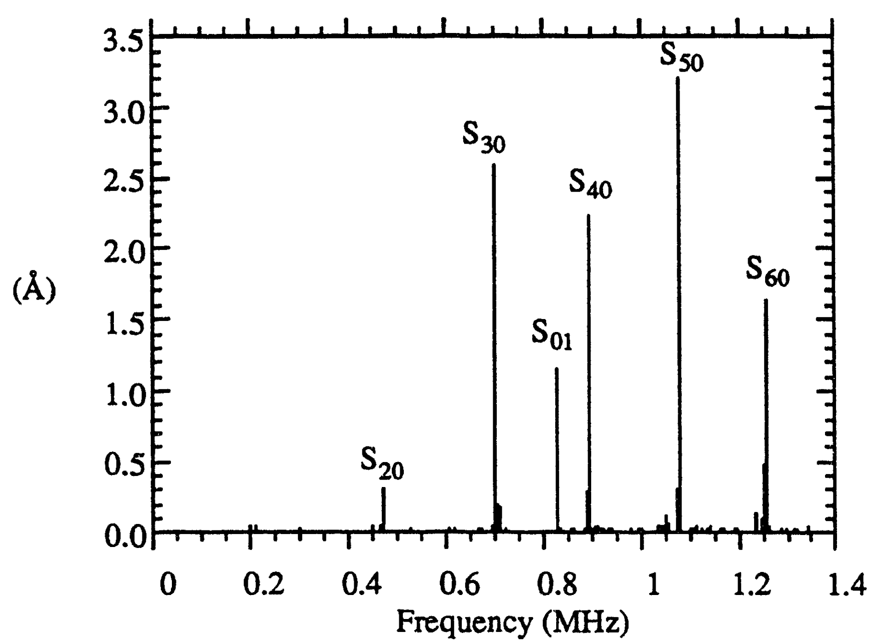

Figure 4.9 Low frequency spectrum of a Si_3N_4 ceramic bearing ball with a diameter of 3/8 inch.

4.3 Experimental Results

4.3.1 Low Frequency Measurement

To verify the results of the contact-contact resonance sphere technique and to qualify the one-point-contact measurement system, we first measured the low frequency spectrum of a 3/8 inch diameter Si_3N_4 ceramic bearing ball. The frequency spectrum in amplitude is shown in figure 4.9. As seen in the figure, only the S_{n0} modes and the S_{0l} modes are visible, while the torsional modes disappear. It is to be noted here that we are using a longitudinal wave transducer, the excitation is normal to the contact surface so no torsional mode should be excited. Even if we excite torsional modes using a shear wave transducer, since torsional wave resonances have no radial motion and their vertical displacement is equal to zero, we will not be able to observe the torsional modes. This is because the interferometer detects only the vertical displacement of the surface. This also demonstrates one of the alignment problems in the contact-contact measurement where we used longitudinal transducers but still observed torsional wave resonances. Comparing to the contact-contact measurement, the one-point contact technique is incapable of observing the torsional modes, but it has considerable advantages in the control of alignment and loading, and yields reproducible results.

4.3.2 High Frequency Measurement

We have also used the technique to operate in the high frequency region to observe surface wave resonances. We measured three Si_3N_4 ceramic bearing balls with a diameter of 1/4 inch. We first measured in the 30 to 35 MHz region where $k_R a \approx 100$. The results are shown in figure 4.10. As we can see in the figure, for the good ball, there is a series of equally spaced peaks. The modulation of the peaks is probably due to the frequency response of the transducer. Balls with cracks have a smaller surface wave resonance amplitude. This is because the cracks are scattering the surface waves. Part of the scattered energy goes into bulk waves and does not contribute to the surface wave resonance. The larger the surface defect, the more energy is converted to bulk waves, causing the decrease of surface wave resonance amplitude.

This interferometer can observe a frequency spectrum from around 10 KHz to about 70 MHz. The limit in the high frequency is due to the physical operating frequency of the Bragg cell. To show this capability, we measured the frequency spectrum of the same three balls from 65 MHz to around 70 MHz. Figure 4.11 shows the result of this measurement.

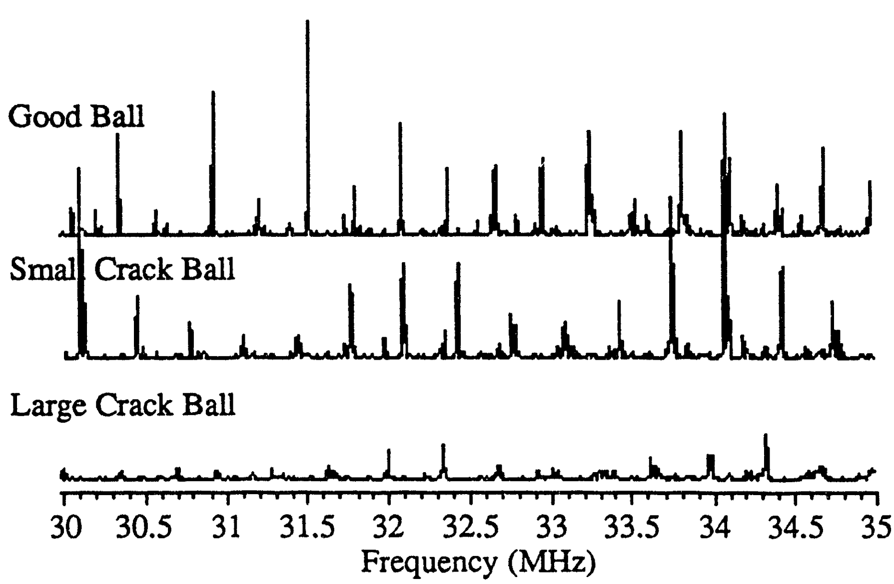

Figure 4.10 Amplitude decrease due to existence of surface defects

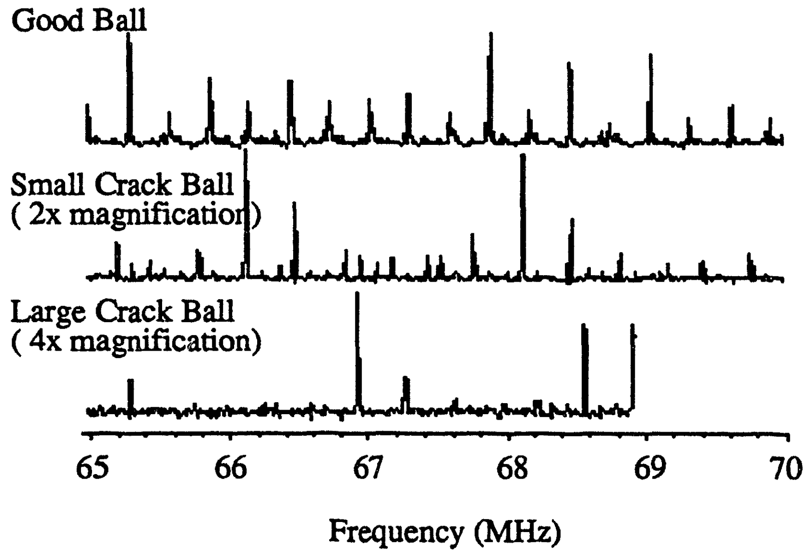

Figure 4.11 Scrambling effect at high frequencies, we see some hybrid modes as well as the disappearance of some modes.

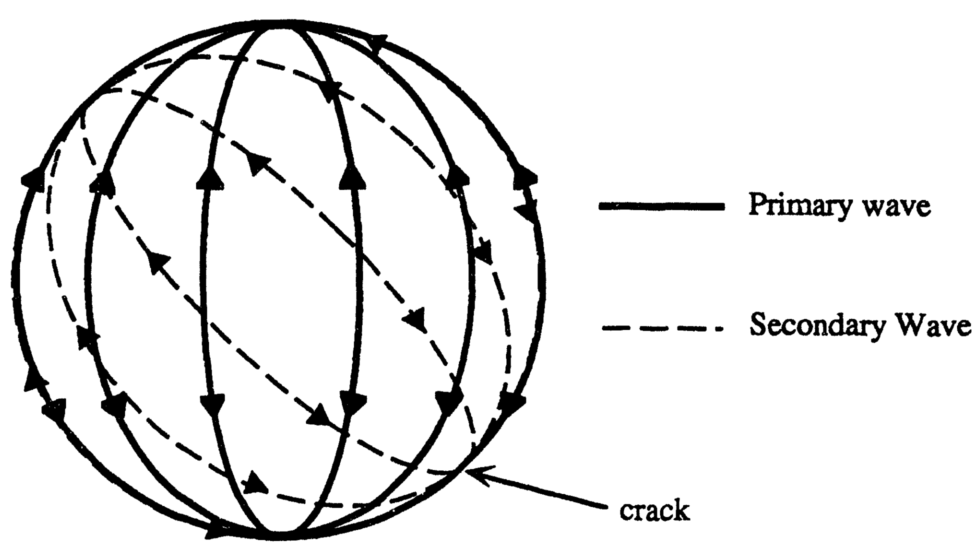

Figure 4.12 Illustration of surface crack as a secondary surface wave source.

In figure 4.11, we again observe a series of equally spaced peaks for the good ball. For balls with defects, figure 4.11 shows a scrambling effect in the higher frequency range. New resonances appear at different frequencies. In this frequency range, surface cracks act like secondary sources of propagation of surface waves. Since waves passing by cracks suffer a phase change and an amplitude change, the primary wave generated by the transducer, and the secondary wave generated by surface cracks, interfere with each other, producing the scrambling effect observed. This phenomenon is illustrated in figure 4.12.

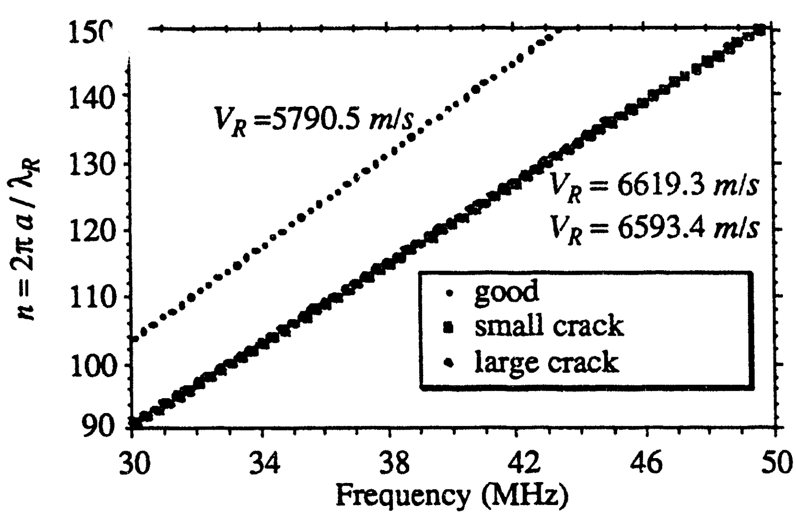

Figure 4.13 Increase in apparent surface wave velocity with existence of surface defect. Curves of the small crack case and the large crack case are almost overlapped.

We also observed another phenomenon, an increase of apparent surface wave velocity with the existence of surface defects. The apparent surface wave velocity V_R is calculated as discussed at the end of chapter 2 where we showed that the circumference of the sphere must be an integral multiple of surface wave length to form surface wave resonance:

$$\text{integer} = m = \frac{2\pi a}{\lambda_R} = \frac{2\pi af}{V_R} . \tag{4.14}$$

Therefore,

$$V_R = \frac{2\pi af}{m} \tag{4.15}$$

where $m = n + 2$ is the number of waves on the sphere.

The reason there is an increase in apparent surface wave velocity with the existence of surface defects is not yet clear. A hypothesis is that some surface waves get scattered back to the source before the waves have propagated one whole circumference. Therefore, the distance travelled becomes shorter, so the measured apparent surface wave velocity is larger. The result is shown in figure 4.13.

Results from the above three figures are useful for non-destructive test. We have shown qualitatively, the effects of surface defects on the resonance spectrum of the balls. If we include our observation from the contact-contact measurement in Chapter 3, we can conclude our observations as (1) decrease in Q, (2) overall decrease in surface resonance peak amplitude, (3) scrambling effect at high frequencies ($k_R\, a \geq 200$), and (4) increase in the apparent surface wave velocity. The second and third phenomena will probably take too long to finish in one experiment, while the first and fourth phenomena seem to be the faster ways to observe the existence of surface defects. For the first phenomenon, we recall the measurement of Q requires curve fitting phase information near resonance using equation (3.17). For the fourth phenomenon, we use equation (4.15) to find the apparent surface wave velocity.

It is necessary to be able to predict surface wave resonance frequencies in order to speed up the measurement. To do this, we have to be able to accurately calculate material properties V_l and V_s in advance. In section 4.3.3, we will discuss the dispersion of surface waves on a sphere. By using V_l and V_s calculated from the low frequency measurement, we can predict each one of the high frequency surface resonance modes and verify with high frequency measurements. In section 4.3.4, we will discuss the dependence of acoustic velocities with temperature. It is useful to establish this dependence relationship to calibrate for high frequency measurement.

4.3.3 Dispersion of Surface Waves on a Sphere

We demonstrate in this section the capability of the one-point-contact technique on small bearing balls. We measured, from 100 KHz to 70 MHz, the resonance spectrum of a good Si_3N_4 bearing ball with a diameter of 1 *mm*. As discussed before, in the low frequency spectrum, we can identify resonant frequencies of bulk resonant modes. We see that this technique, unlike the contact technique, excites only spheroidal modes. This is because there is only one point of contact, and the excitation direction is in the normal direction of the contact. It also helps to explain the alignment difficulty for the contact-

contact technique where we observed torsional modes. We chose two high Q spheroidal modes to calculate material properties of the 1 mm diameter sphere using equation (2.26). The results are shown in Table 4.1. The calculated values of V_l and V_s were then used to calculate the dispersion curve of surface waves using equation (2.26). For each positive integer n, the first solution to equation (2.26) is mode S_{n0}, which corresponds to surface wave resonance mode (there is no surface wave resonance mode solution for $n = 1$). For n larger than 100, the equation asymptotically approaches that of the Rayleigh wave characteristic equation as discussed in section 2.2.3.

The calculated surface wave dispersion curve is then compared to the experimentally measured surface wave resonances, as seen in figure 4.13. The theoretical prediction and measurement agree with each other very well. Each one of the surface wave mode is predicted and measured. This means if we know V_l and V_s accurately, we should be able to predict where the high frequency resonance modes are. We also see that the apparent surface wave velocity asymptotically approaches a constant—true Rayleigh wave velocity. As shown in figure 4.14, V_R starts approaching a constant when $k_R\, a \geq 40$.

ν (Poisson's Ratio)	V_l (m/s)	V_S (m/s)	V_R (m/s)
0.26646	10999	6206.1	5772.6

Table 4.1 Material properties of a ceramic bearing ball with a diameter 1mm, calculated from two high Q spheroidal modes.

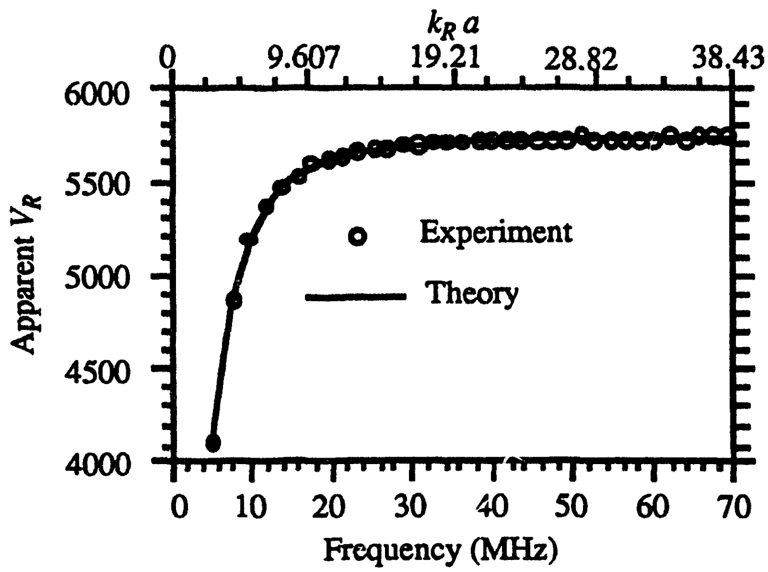

Figure 4.14 Dispersion relation of surface waves on a sphere.

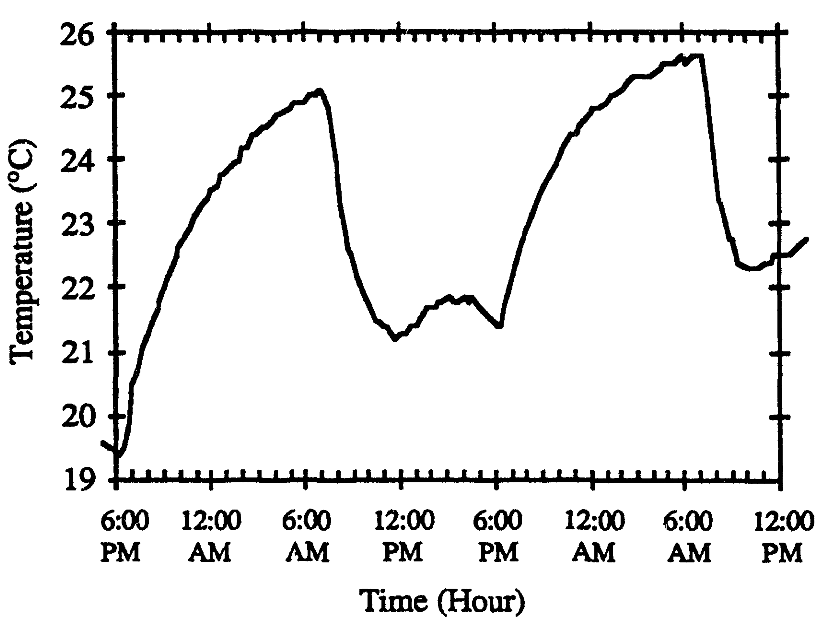

Figure 4.15 Temperature changes in the laboratory.

4.3.4 Temperature Calibration

In section 4.3.2 we discussed the necessity to get accurate numbers for V_l and V_s. In this section, the optical probing technique is used to observe the change in acoustic velocities with respect to temperature variation. Figure 4.15 illustrates the temperature changes in the laboratory within a 42-hour time period.

For a laboratory temperature variation between 19°C and 26°C, we continuously measured two high Q spheroidal modes. We then used these two modes to calculate V_s and V_l. Figures 4.16 and 4.17 show the calculated velocity-temperature relationship. In figure 4.16,

$$\begin{cases} V_l = 11177 - 0.15524T \\ \dfrac{1}{V_l}\dfrac{dV_l}{dT} = -1.38892 \cdot 10^{-5} - 1.92911 \cdot 10^{-10} T \end{cases} \tag{4.16}$$

and from figure 4.17,

$$\begin{cases} V_s = 6322.8 - 0.087853T \\ \dfrac{1}{V_s}\dfrac{dV_s}{dT} = -1.38946 \cdot 10^{-5} - 1.93061 \cdot 10^{-10} T \cdot \end{cases} \tag{4.17}$$

Combining equations (4.16), (4.17), and (2.12), it can be shown that Poisson's ratio is:

$$\nu = 0.264691 + 3.73871 \times 10^{-9} T. \tag{4.18}$$

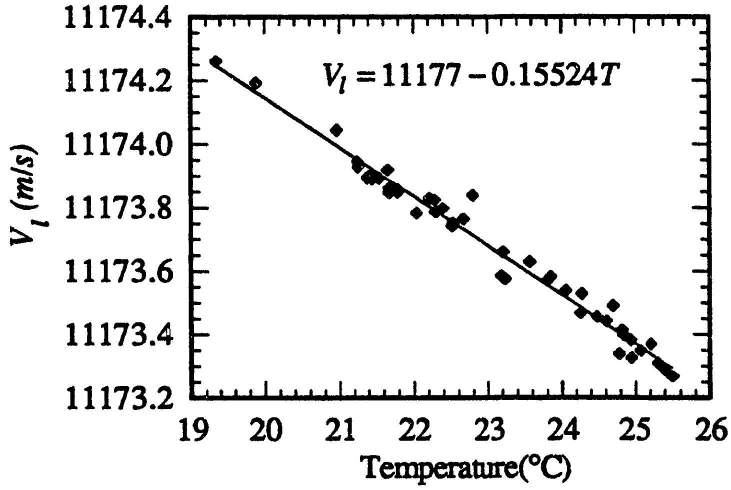

Figure 4.16 Longitudinal wave velocity change versus laboratory temperature change for Si_3N_4 material.

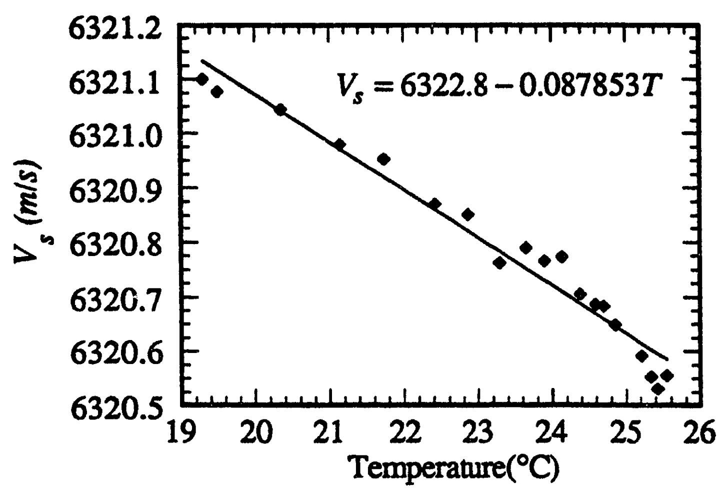

Figure 4.17 Shear wave velocity change versus laboratory temperature change for Si_3N_4 material.

Also, combining equations (4.16), (4.17), and (2.15), it can be shown that the Rayleigh wave velocity is:

$$V_R = 5828.18 - 0.0809767T. \tag{4.19}$$

Equations (4.16), (4.17), and (4.19) all show a decrease in acoustic velocity with an increase in temperature. This phenomenon can be explained by the following physical interpretation. Acoustic velocity is equal to the square root of stiffness divided by density. As temperature increases, the material becomes softer and the stiffness decreases, also, the density decreases due to thermal expansion. Therefore, as temperature increases, the acoustic velocity decreases. The ordinates of figures 4.16 and 4.17 also show the high degree of accuracy in our measurement.

The above argument is verified by calculating the dependence of stiffness constants $c_{11} = \lambda + 2\mu$ and $c_{44} = \mu$, where λ and μ are the Lamé constants[29]. The theoretical value for density of Si_3N_4 ceramic material is 3270 Kg/m^3. Combining equations (4.16) and (4.17) and

$$\begin{cases} V_l = \sqrt{\dfrac{c_{11}}{\rho}} \\ Vs = \sqrt{\dfrac{c_{44}}{\rho}} \end{cases}, \tag{4.20}$$

we get

$$\begin{cases} \dfrac{dc_{11}}{dT} = -1.13477 \cdot 10^7 + 157.610T \\ \dfrac{dc_{44}}{dT} = -3.63282 \cdot 10^6 + 50.4767T \end{cases} \tag{4.21}$$

4.4 Concluding Remarks

In this chapter, we demonstrated a new technique capable of measuring the material properties of spherical objects, and capable of inspecting them for the presence of surface defects. The technique uses a single point contact to excite resonances in the object and an optical interferometer to measure these resonances. The measurement can be made on spherical objects of any size and over an unlimited frequency range. We also showed, for the first time, good agreement between theory and experiment for the dispersion relation of surface waves on a sphere. This technique has the potential of inspecting nonmetallic spheres, or spheres with coatings, and cylindrical objects. It may also be applied to objects of uncommon geometries.

REFERENCES

[1] S. P. Timoshenko and J. N. Goodier, *Theory of Elasticity*, 3rd Edition, McGraw-Hill Book Company (1970).

[2] D. Royer, E. Dieulesaint, X. Jia, and Y. Shui, Optical Generation and Detection of Surface Acoustic Waves on a Sphere, Appl. Phys. Lett. **52** (17) (1988).

[3] Dr. Chris Scrub, Manager, Manufacturing NDT, The National NDT Centre, Harwell Laboratory, Oxfordshire OX11 ORA, private communication

[4] Jean-Pierre Monchalin, *Optical Detection of Ultrasound*, in *IEEE Transactions on Ultrasonics, Ferroelectrics, and Frequency Control*, **UFFC-33**, No. 5. (September 1986).

[5] G. I. Stegeman, *Optical Probing of Surface Waves and Surface Wave Devices*, IEEE Trans. Sonics Ultrason., **SU-23** (1976)

[6] R. Adler, A. Korpel, and P. Desmares, An instrument for making surface waves visible, IEEE Trans. Sonics. Ultrason., SU-15 (1967)

[7] G. Alers, M. A. Tennison, R. B. Thompson, and B. R. Tittmann, *Visualization of Surface Elastic Waves on Structural Materials*, Ultrasonics, **11**, (1973)

[8] H. Engan, *Phase Sensitive Laser Probe for High-Frequency Surface Acoustic Wave Measurements*, IEEE Trans. Sonics. Ultrason., **SU-25**, (1978)

---

[9] H. Sontag and A. C. Tam, *Optical Detection of Nanosecond Acoustic Pulses*, IEEE Trans. Ultrason., Ferroelectrics, Freq Contr. **UFFC-33**, (5), (1986).

[10] M. A. Olmstead and N. M. Amer, *A New Probe of the Optical Properties of Surfaces*, J. Vac. Sci. Technol, **B1**, (1983)

[11] J. Opsal, A. Rosencwaig, and D. L. Willenborg, *Thermal-Wave Detection and Thin-Film Thickness Measurements with Laser Beam Deflection*, App. Opt. 22, (1983).

[12] G. I. Stegeman, *Optical Probing of Surface Waves and Surface Wave Devices*, IEEE Trans. Sonics Ultrason., **SU-23** (1976)

[13] R. L. Whitman and A. Korpel, *Probing of Acoustic Surface perturbations by coherent light*, App. Opt. **8**, (1969)

[14] C. Thomsen, H. T. Grahn, H. J. Maris, and J. Taue, *Ultrasonic Experiments with Picosecond Time Resolution*, J. Physique, colloque C10, suppl, **46**, (1985)

[15] Wolf Bickel, *Method and Apparatus for Receiving Ultrasonic Waves by Optical Means*, U. S. Patent #4,129,041, Dec. 1978, assigned to Krautkrämer-Branson Inc.

---

[16] Wolf Bickel, *Method and Apparatus for Receiving Ultrasonic Waves by Optical Means*, U. S. Patent #4,129,041, Dec. 1978, assigned to Krautkrämer-Branson Inc.

[17] Wolf Bickel, *Method and Apparatus for Receiving Ultrasonic Waves by Optical Means*, U. S. Patent #4,345,475, Aug. 1982, assigned to Krautkrämer-Branson Inc.

[18] G. A. Massey and R. R. Carter, *Portable Laser Instrument for Vibration Analysis and Transducer Calibration*, Shock and Vibration Bull. **37**, part 2, (1968)

[19] P. Buchhave, *Laser Doppler Vibration Measurements Using Variable Frequency Shift*, DISA Informat., no. 18, (1975)

[20] G. Bouchard and D. B. Bogy, *Experimental Measurement of Scattered Surface Waves Using a Laser—Doppler Technique*, J. Acoust. Soc. Amer, **77**, (1985)

[21] J. P. Monchalin, *Optical Detection of Ultrasound at a Distance*, Can. J. Soc. Nondestructive Testing, **6**, (1984).

[22] R. L. Whitman, L. J. Laub, and W. Bates, *Acoustic Surface Displacement Measurements on a Wedge-Shaped Transducer Using an Optical Probe Technique*, IEEE Trans. Sonics Ultrason. **SU-15**, (1968)

[23] R. Dändliker and J. F. Willemin, *Measuring Microvibrations by Heterodyne Speckle Interferometry,* Optics Lett. **6**, (1981)

[24] C. H. Palmer andR. O. Claus, *Application of Optical Fibers to Wideband Differential Interferometry*, Mat. Eval, **41**, (1983)

[25] L. M. Barker, *Laser Interferometry in Shock-Wave Research*, Exp. Mech., (May, 1972)

[26] W. Kaule, *Interferometric Method and Apparatus for Sensing Surface Deformation of a Workpiece Subjected to Acoustic Energy*, U. S. patent #4,046,477, Sept. 1977, assigned to Krautkrämer-Branson Inc.

[27] D. Royer and E. Dieulesaint, *Optical Probing of the Mechanical Impulse Response of a Transducer*, Appl. Phys. Lett. **49** (17) (1986)

[28] G. S. Kino, *Acoustic Waves: Devices, Imaging, and Analog Signal Processing* Prentice-Hall, New Jersey, (1987).

[29] B. A. Auld, *Acoustic Fields and Waves in Solids,* Vol. 1, 2nd ed., Robert E. Krieger Publishing Company, Malabar, Florida, (1990)

Chapter 5

Conclusion

In this dissertation, we started by discussing the importance of inspecting ceramic bearing balls. We studied the theory of wave propagation on spheres and analyzed how these waves build up resonances on spheres. It was shown that there are two types of resonances on a sphere. The first type is the torsional resonances. Their resonant frequencies are dependent only on geometry and shear wave velocity of the material. The second type is the spheroidal resonances. Their resonant frequencies are dependent on geometry, shear wave velocity, and longitudinal wave velocity of the material. One special case of the spheroidal resonances is the pure compressional resonances. Another special case of the spheroidal resonances is the surface acoustic wave resonances at high frequencies. Surface waves are shown to propagate along great circles of the sphere, and have focus to a 3 dB spot size of only 0.364 surface wavelength.

The contact-contact resonance sphere technique demonstrated its capability of measuring material properties at low frequencies. We also discussed the fact that there is no correlation between the low frequency spectrum and the crack size. At high frequencies, we observed the existence of surface wave resonances. This is one of the major breakthrough of this research project. At the same time, we observed qualitatively the relationship between crack size and surface wave resonance quality factor.

The continuation of the application of the contact-contact resonance sphere technique is the one-point-contact technique. With one single point contact, we successfully excited surface wave resonance. The optical detection scheme, using a heterodyne interferometer, eliminates external environmental interference with the resonance of the sphere. This technique enables one to perform measurement at even higher frequency region, which in turn allows the generation of surface waves on smaller spheres. We reported several observations of the effects of surface defects on the resonance spectrum. We also demonstrated the high degree of accuracy of this technique by reporting the small dependence of acoustic velocities with temperature. In addition, we showed, for the first time, excellent agreement between theory and experiment for the dispersion relation of surface waves on a sphere.

The laser-ultrasound measurement can be made on spherical objects of any size and over an unlimited frequency range. This technique has the potential of inspecting nonmetallic spheres, spheres with coatings, and cylindrical objects. It can also be applied to objects of uncommon geometries.

Future development and potential application of this research project will be multi-directional. First of all, it is important to establish a theoretical model that describes the effect on the resonance spectrum of different types of surface defects. It would then be helpful to select the best technique to obtain high measurement speed. Second, it would be interesting to be able to excite a high frequency surface wave pulse. We actually tried to do this using the current transducer. However, due to the small contact area, we were unable to generate a strong enough pulse to be observable. Therefore, it is desirable to design another transducer which can generate a stronger surface wave pulse on the sphere by changing its material (buffer rod) and geometry (radius of the hemispherical bowl).

To adapt to industrial applications, it would be quite feasible to build a number of transducer-interferometer system in parallel for multiple ball inspection. The advantage of not needing realignment of the optical system makes this technique attractive for multiple ball inspection, since it will definitely speed up the entire quality control process

DATE FILMED

5/17/94

END